A New Open-Source Nuclear Equation of State Framework based on the Liquid-Drop Model with Skyrme Interaction

A. S. Schneider,[1,*] L. F. Roberts,[2,†] and C. D. Ott[1,3,‡]

[1]*TAPIR, Walter Burke Institute for Theoretical Physics, MC 350-17, California Institute of Technology, Pasadena, CA 91125, USA*

[2]*National Superconducting Cyclotron Laboratory and Department of Physics and Astronomy, Michigan State University, East Lansing, MI 48824, USA*

[3]*Center for Gravitational Physics and International Research Unit of Advanced Future Studies, Yukawa Institute for Theoretical Physics, Kyoto University, Kyoto, Kyoto Prefecture 606-8317, Japan*

(Dated: July 7, 2017)

The equation of state (EOS) of dense matter is an essential ingredient for numerical simulations of core-collapse supernovae and neutron star mergers. The properties of matter near and above nuclear saturation density are uncertain, which translates into uncertainties in astrophysical simulations and their multi-messenger signatures. Therefore, a wide range of EOSs spanning the allowed range of nuclear interactions are necessary for determining the sensitivity of these astrophysical phenomena and their signatures to variations in input microphysics. We present a new set of finite temperature EOSs based on experimentally allowed Skyrme forces. We employ a liquid drop model of nuclei to capture the non-uniform phase of nuclear matter at sub-saturation density, which is blended into a nuclear statistical equilibrium EOS at lower densities. We also provide a new, open-source code for calculating EOSs for arbitrary Skyrme parametrizations. We then study the effects of different Skyrme parametrizations on thermodynamical properties of dense astrophysical matter, the neutron star mass-radius relationship, and the core collapse of 15 and 40 solar mass stars.

PACS numbers: 21.65.Mn,26.50.+x,26.60.Kp

I. INTRODUCTION

Core-collapse supernovae (CCSNe) and neutron star (NS) mergers, the birth places of neutron stars and black holes (BH), can only be understood in the light of the microphysics that drives them. A clear picture of these astrophysical phenomena is directly tied to our understanding of the properties of matter and radiation at high energy densities. Therefore, one of the essential microphysical ingredients in computational simulations of these phenoma is the equation of state (EOS) of dense matter (e.g., [1, 2]).

An EOS for CCSNe and NS merger simulations must encompass a very large range in density, temperature, and composition. The temperatures encountered in these events range from zero up to hundreds of MeV, densities from $\lesssim 10^4$ to $10^{15}\,\mathrm{g\,cm^{-3}}$, and proton fractions y may be close to zero or as high as 0.60. Over this wide parameter space, matter may be in a gas, liquid, or solid phase, and in its ground state or in a highly-excited state [1–3].

At low densities and temperatures, isospin symmetric matter with the same number of protons and neutrons clusters into heavy nuclei. By making the system isospin asymmetric, *i.e.*, having an excess of neutrons with respect to protons or vice-versa, nuclei become neutron or proton rich. If the isospin asymmetry is large enough, nucleons drip out of nuclei to form a background gas. Keeping proton fraction and density constant, heavy nuclei split into lighter ones as the temperature is increased. At very high temperatures all nuclei dissociate and only a gas of free nucleons immersed in the electron and photon gas exists. If, instead, composition and temperature are kept constant as density is increased, nuclei become more and more packed. Just below nuclear saturation density, a series of phase transitions in which nucleons arrange themselves into complex shapes known as nuclear "pasta" occurs [4, 5]. At even higher densities, nucleons form a free gas and the EOS stiffens due to short range nuclear repulsive forces. The EOS may soften at densities much higher than nuclear saturation density due to the appearance of heavier leptons, hyperons, kaon condensates, or a quark-gluon plasma [6–8]. We do not consider these phases in the present work.

The EOS is poorly constrained in regions of parameter space relevant for CCSNe and NS mergers, as matter in these sites is under extreme conditions that cannot be easily reproduced in laboratory experiments. Hence, any EOS built for astrophysical applications depends on extrapolations based on theoretical models of microscopic interactions as well as astrophysical and experimental inputs. Ideally, these models should be supported by available nuclear experimental data [9, 10] and make predictions that fulfill known astrophysical [11–16] and theoretical constraints [17–19].

Broadly, there are two approaches for generating nuclear interactions used in calculating the properties of dense matter. Phenomenological interactions employ reasonable forms for the nuclear interaction and fit the force parameters to the measured properties of nuclei and other constraints from laboratory experiments [20–23] and astrophysical observations of NSs [24]. Since they are constrained mainly by observations of nearly isospin-symmetric systems accessible in the laboratory, extrapolating to the highly isospin-asymmetric

*Electronic address: andschn@caltech.edu
†Electronic address: robertsl@nscl.msu.edu
‡Electronic address: cott@tapir.caltech.edu

matter encountered in NS mergers and CCSNe introduces significant uncertainties. More microscopic treatments, such as chiral effective field theory, use interactions that obey symmetries of QCD and fit the small number of free parameters in the interaction based on observed properties of the nucleon-nucleon interaction [25]. These approaches are very accurate at near nuclear saturation density and below and should capture the properties of highly asymmetric matter, but difficult to calculate higher-order interactions become increasingly important with increasing density [26].

Another source of uncertainty, in addition to the uncertainty in the form of the effective nuclear interaction, comes from the many-body techniques used to predict the thermodynamic properties of an ensemble of nucleons. For a given effective nuclear interaction, the properties of a system of nucleons can be calculated exactly using modern quantum many-body techniques [27, 28], but such calculations are too expensive to cover the wide range of conditions required for an astrophysical EOS [28, 29]. Because of their relative simplicity and their ability to capture the properties of nuclear matter near saturation density, phenomenological interactions combined with mean-field techniques are often applied when calculating astrophysical EOSs [3, 24, 30]. For instance, phenomenological Skyrme models assume a zero-range effective interaction that, in the mean field approximation[1], results in a parametrized energy functional that can be fit to measured properties of nuclei [31].

Non-uniform phases of matter appear at low temperatures and sub-saturation densities, with a high-density phase near nuclear saturation density and a low density nucleon gas phase. The treatment of these non-uniform phases is another source of uncertainty in a high-density astrophysical EOS. A number of different approaches for treating the non-uniform phases have been used in previous work (in addition to using different treatments of uniform nuclear matter). For a review, see Oertel *et al.* [1] and references therein.

One often used approach is to treat the non-uniform nuclear matter using the single nucleus approximation (SNA) [3, 30, 32–38]. The SNA assumes that there is one representative nucleus (or, more generally, a high density structure such as a pasta phase) and calculates its properties from equilibrium conditions within a spherical Wigner-Seitz cell, possibly including surface, Coulomb, and translational energy corrections using either a liquid drop or a Thomas-Fermi model for the surface corrections. At very low temperature this should be a good approximation, but at intermediate temperatures an ensemble of nuclei is likely to be present.

A second approach is to use a nuclear statistical equilibrium (NSE)-like description of nuclei along with Coulomb corrections and exclude the low density gas from regions inside the nuclei [24, 39–44]. This gives a more reasonable distribution of nuclei at finite temperature and the excluded volume approximation makes nuclei naturally dissappear just below saturation density. However, such approaches cannot easily incorporate the presence of nuclear pasta and may have trouble including the exotic nuclei formed at very high density. Additionally, a number of works have used a hybrid approach where NSE is used at low density and the SNA is used closer to nuclear saturation density [45–49].

Motivated by the need for a wide array of finite-temperature nuclear EOSs consistent with experimental and observational constraints, we build an open-source code to construct EOSs for wide range of Skyrme interactions available in the literature and use the code to generate EOS tables using broad range of Skyrme interactions. For the inhomogeneous phase, we follow the open-source model of Lattimer & Swesty [3] (hereafter referred to as L&S; available at `http://www.astro.sunysb.edu/dswesty/lseos.html`) at high density and transition to an NSE model at low-density. We extend the L&S model to include non-local isospin asymmetric terms, treat the size of heavy nuclei consistently, and include an improved method to treat nuclear surfaces. Rather than use a Gibbs construction to go from inhomogeneous to homogeneous nuclear matter, we simplify the treatment and choose either the uniform or non-uniform phase based on which has a lower free energy, which sets the phase transition to be first order. Additionally, the algorithm used in the new EOS code converges across a much wider range of temperature, density, composition space than the original L&S code. At very high densities, we allow for additional terms in the Skyrme parametrization that can be used to stiffen the high-density EOS while leaving the saturation-density EOS essentially unchanged. This allows one to use a specific Skyrme parametrization that agrees with well determined nuclear matter constraints, but varies the maximum NS mass.

We thoroughly test our new EOSs to ensure thermodynamic consistency. Using the LS220 parametrization, we find excellent agreement with the original work of L&S. We present zero-temperature NS mass-radius relations for all considered Skyrme parametrizations and demonstrate how the new high-density adjustments translate to NS structure. Finally, we employ the open-source general-relativistic `GR1D` code [50–52] to carry out spherically-symmetric core collapse and postbounce supernova simulations with our new EOSs. We consider 15 solar-mass and 40 solar-mass pre-supernova stars and follow the 40 solar-mass simulations to black hole formation. Burrows & Lattimer [53] argued that thermodynamic quantities obtained in the SNA approximation differ little from the general case. Nonetheless, we find that these differences have a large impact on some EOS properties and in our core collapse simulations. Importantly, we find that the radius of the stalled postbounce supernova shock is systematically lower in simulations using SNA at low densities than in simulations employing NSE. This may have important implications for the efficacy of the neutrino-driven CCSN explosion mechanism in multi-dimensional simulations.

The remainder of this paper is organized as follows. In Sections II and III we review, respectively, the formalism to ob-

[1] The mean field approximation assumes that nucleons only interact with other nucleons through the average field produced by all of the other nucleons, removing the possibility of any correlations from the system.

tain the EOS in the SNA and the methodology to solve the system of equations that minimize the free energy of nuclear matter. We compare the results of our code to those of L&S in Section IV. In the same section, we compare EOSs obtained from different Skyrme parametrizations, as well as nuclear matter properties obtained for selected Skyrme parametrizations. In Section V, we study properties of cold NSs obtained for different Skyrme parametrizations and the effects to NS mass-radius curve obtained from adding extra stiffening terms to the EOS. We then briefly study adiabatic compression of nuclear matter in Section VI and spherical core collapse of 15 and 40 solar mass stars in Section VII. Due to its relevance for core collapse, in Section VII A, we discuss an implementation of an NSE EOS and a method to transition from the SNA EOS at high densities to NSE at low densities. Finally, we conclude in Section VIII. In the appendices, we provide details left out in the main text, including the lepton and photon contributions and details on our NSE treatment. The EOS source code and example EOS tables are available at https://stellarcollapse.org/SROEOS.

Throughout this paper, we use the convention of measuring temperature in MeV, setting the Boltzmann constant $k_B = 1$ unless otherwise explicitly mentioned. For thermodynamic quantities, we use upper case letters when refering to quantities per volume and lower case letters for specific (per baryon or per mass) quantities. Furthermore, we define the zero point of the specific internal energy based on the free neutron rest mass m_n, set the neutron and proton masses m_n and m_p to their experimental values unless otherwise noted, and explicitly include the neutron–proton mass difference where necessary. Finally, we use the neutron mass m_n to convert from number density (fm^{-3}) to rest-mass density ($\mathrm{g\,cm}^{-3}$).

II. SINGLE NUCLEUS APPROXIMATION FORMALISM

Here, we describe the formalism we use for determining a self-consistent EOS from a given Skyrme parametrization across a wide range of density n, temperature T and proton fraction y. At high density, our model closely follows L&S [3], while at lower densities we employ an NSE EOS, which we describe in Section VII A. We assume that the medium contains neutrons, protons, alpha particles, electrons, positrons, and photons. The electrons, positrons, and photons are treated as uniform free gases and charge neutrality is assumed, so that the number of electrons per baryon is equal to the number of protons per baryon. Electron/positron and photon contributions are discussed in detail in Appendix A. In what follows, *nucleonic matter* refers to a bulk system of protons and neutrons with uniform density. We use *uniform matter* to refer to a free gas of nucleons and alpha particles, while we use *non-uniform matter* to describe matter including heavy nuclei.

The possible presence of heavy nuclei or pasta-like phases at high density is treated via the single nucleus approximation (SNA), which is essentially a two-phase construction including surface effects. In this construction, each heavy nucleus occupies a volume V_N inside a Wigner-Seitz cell of volume $V_{\rm cell}$. We define the volume fraction occupied by heavy nuclei as $u = V_N/V_{\rm cell}$. In the interior of the heavy nucleus, nucleonic matter is assumed to have a constant density (n_i) and proton fraction (y_i), and have thermodynamic properties determined from a Skyrme interaction in the mean field approximation. In each cell, nuclei are surrounded by a free gas of nucleons and alpha particles that occupy a volume $V_{\rm cell} - V_N$. The alpha particles have density n_α and are assumed to be hard spheres of volume $v_\alpha = 24\,\mathrm{fm}^{-3}$ [35] that exclude nucleons, so that they occupy a fraction $n_\alpha v_\alpha$ of the exterior volume. This leaves a fraction of the total cell volume $u_o = (1-u)(1-n_\alpha v_\alpha)$ for the exterior nucleons. They have a density n_o and a proton fraction y_o in this volume. The nucleons in the exterior portion of the cell are treated using the same Skyrme interaction as the material inside the nucleus. With these definitions, we can write the total baryon and proton number densities as

$$n = u n_i + (1-u)[4n_\alpha + n_o(1-n_\alpha v_\alpha)]\,, \tag{1a}$$

$$ny = u n_i y_i + (1-u)[2n_\alpha + n_o y_o(1-n_\alpha v_\alpha)]\,. \tag{1b}$$

When $u \to 0$, uniform matter consisting of neutrons, protons, and alpha particles is recovered. All of the material is assumed to be in thermal equilibrium and it is therefore characterized by a single temperature T.

The Helmholtz free energy of the system, from which all other thermodynamical quantities may be derived, is the sum of free-energies of the individual components, that is,

$$F = F_o + F_\alpha + F_h + F_e + F_\gamma\,, \tag{2}$$

where F_o, F_α, F_h, F_e, and F_γ are, respectively, the free-energy densities of the nucleon gas outside the heavy nuclei, alpha particles, nucleons clustered into heavy nuclei, electrons and positrons, and photons. The free energies of the leptons and photons are simply those of arbitrarily degenerate and relativistic free gases (see Appendix A for details). The alpha particles are treated as a free Boltzmann gas present only in the exterior volume, so that their contribution to the free energy is given by

$$F_\alpha = (1-u) n_\alpha (\mu_\alpha - B_\alpha - T)\,, \tag{3}$$

where B_α is the alpha particle binding energy[2]. The alpha particle chemical potential is

$$\mu_\alpha = T \ln\left(\frac{n_\alpha}{8 n_Q}\right)\,, \tag{4}$$

where $n_Q = (m_n T/2\pi\hbar^2)^{3/2}$. The exterior nucleon contribution to the free energy is

$$F_o = u_o n_o f_B(n_o, y_o, T)\,, \tag{5}$$

[2] Unless otherwise noted, we set the binding energy of the alpha particles to the experimentally measured value, $B_\alpha = 30.887\,\mathrm{MeV}$. This follows the discussion of Horowitz and Schwenk [54] that noticed that L&S set particle energies with respect to the neutron vacuum mass, but did not include the neutron-proton mass difference in their calculations for the alpha particle binding energy.

where f_B is the specific free energy of a bulk nucleon gas (nucleonic matter), which is assumed to come from a particular model for the properties of bulk nuclear matter. In this work, we assume that bulk nuclear matter is described by Skyrme interactions in the mean field approximation as is discussed in the Section II A.

The free energy density of the heavy nuclei is further decomposed as

$$F_h = F_i + F_S + F_C + F_T, \tag{6}$$

where F_i, F_S, F_C, and F_T are, respectively, the free energy densities due to the assumed interior bulk nucleon gas, surface effects, Coulomb forces, and bulk translational motion of the heavy nuclei. The free energy density of bulk nucleons inside nuclei is $F_i = u_i n_i f_i$, where $f_i \equiv f_B(n_i, y_i, T)$ and u_i is the total heavy nuclei volume. Ignoring the surface volume, $u_i = 1 - u_o$. If the surface, Coulomb, and translational contributions to the free energy are neglected, we would arrive at a Gibbs two phase construction. These finite size contributions are important for recovering a semi-realistic description of nuclei and the pasta phases and we describe the models we use for them below in Sections II B – II D after discussing bulk nuclear matter in the next Section II A.

A. Bulk nuclear matter

Assuming a Skyrme type interaction in the mean field approximation, the internal energy density E_B of nucleonic matter with density n, proton fraction y, and temperature T can be written in the form[3]

$$\begin{aligned} E_B(n,y,T) =& \frac{\hbar^2\tau_n}{2m_n^*} + \frac{\hbar^2\tau_p}{2m_p^*} + (a + 4by(1-y))\, n^2 \\ &+ \sum_i (c_i + 4d_i y(1-y))\, n^{1+\delta_i} - yn\Delta\,, \end{aligned} \tag{7}$$

where a, b, c_i, d_i, and δ_i are parameters of the Skyrme force and τ_t ($t \in \{n, p\}$) are the kinetic energy densities of neutrons and protons. We include in Equation (7) a summation over index i in the fourth term as introduced by Agrawal *et al.* [55]. The first two right-hand side terms represent the non-relativistic kinetic energy density of neutrons n and protons p, respectively. The term proportional to n^2 represents two-body nucleon interactions while the terms proportional to $n^{1+\delta_i}$ approximate the effects of many-body or density dependent interactions. The last right-hand size term includes the mass difference between neutrons and protons $\Delta = m_n - m_p$, since we measure all energies relative to the free neutron rest mass m_n. The kinetic energy terms depend on the density-dependent effective nucleon masses m_t^* given by

$$\frac{\hbar^2}{2m_t^*} = \frac{\hbar^2}{2m_t} + \alpha_1 n_t + \alpha_2 n_{-t}\,. \tag{8}$$

Here, m_t is the vacuum nucleon mass and $-t$ denotes the opposite isospin of t. The quantities α_1 and α_2 are also parameters of the model. Additional terms that mix the neutron and proton densities in Equation (8), as used by Chamel *et al.* [56], are omitted here.

The temperature dependence of the nuclear force is implicitly included in the τ_t term,

$$\tau_t = \frac{1}{2\pi^2}\left(\frac{2m_t^* T}{\hbar^2}\right)^{\frac{5}{2}} \mathcal{F}_{3/2}(\eta_t)\,, \tag{9}$$

where the Fermi integral $\mathcal{F}_k(\eta)$ is given by

$$\mathcal{F}_k(\eta) = \int_0^\infty \frac{u^k du}{1 + \exp(u - \eta)}\,. \tag{10}$$

The Fermi integral is a function of the degeneracy parameter

$$\eta_t = \frac{\mu_t - V_t}{T}\,. \tag{11}$$

Here, μ_t is the nucleon chemical potential and V_t is the single-particle potential,

$$V_t \equiv \left.\frac{\delta\epsilon_B}{\delta n_t}\right|_{\tau_t,\tau_{-t},n_{-t}}\,. \tag{12}$$

The degeneracy parameter η_t can be obtained from the nucleon density and temperature by inverting the relation

$$n_t = \frac{1}{2\pi^2}\left(\frac{2m_t^* T}{\hbar^2}\right)^{\frac{3}{2}} \mathcal{F}_{1/2}(\eta_t)\,. \tag{13}$$

We obtain the Fermi integrals and their inverses using the routines provided by Fukushima [57, 58]. These proved to be fast, accurate and thermodynamic consistent.

In Equations (7) and (8), a, b, c_i, d_i, δ_i, α_1, and α_2 are parameters of the model that are chosen to reproduce observables of infinite nuclear matter, an idealized system of many nucleons interacting only through nuclear forces. These parameters are directly related to the more often used Skyrme parameters x_j and t_j ($j \in \{0, 1, 2\}$), t_{3i} and σ_i through [9, 59]

$$a = \frac{t_0}{4}(1 - x_0)\,, \tag{14a}$$

$$b = \frac{t_0}{8}(2x_0 + 1)\,, \tag{14b}$$

$$c_i = \frac{t_{3i}}{24}(1 - x_{3i})\,, \tag{14c}$$

$$d_i = \frac{t_{3i}}{48}(2x_{3i} + 1)\,, \tag{14d}$$

$$\delta_i = \sigma_i + 1\,, \tag{14e}$$

$$\alpha_1 = \frac{1}{8}\left[t_1(1 - x_1) + 3t_2(1 + x_2)\right]\,, \tag{14f}$$

$$\alpha_2 = \frac{1}{8}\left[t_1(2 + x_1) + t_2(2 + x_2)\right]\,. \tag{14g}$$

[3] In principle, contributions of spin-orbit and Coulomb interaction terms should also be included in the equation for the internal energy E_B. However, since they constitute only a small portion of the total energy, we neglect them.

For most Skyrme parametrizations, t_{3i}, x_{3i}, and σ_i are only non-zero for a single value of i, which we set to $i = 1$. Even limiting i to a single value $i = 1$, we note that if we compare Equation (7) with Equation (2.8) of L&S, we have an extra term, the one proportional to the parameter d_1. This term is necessary to obtain the correct EOS whenever $x_{31} \neq -1/2$. This is the case for almost every Skyrme parametrization found in the literature, albeit not for that of L&S.

L&S obtain the parameters of the bulk internal energy density (Equation 7) from experimentally determined values for symmetric matter at saturation density n_0, the binding energy E_0, the incompressibility K_0, and the symmetry energy at saturation J. We implement three different methods to determine the parameters of Equation 7:

1. Following L&S, input experimental values for n_0, E_0, K_0, and J, which are then used to determine a, b, c and δ. For consistency with L&S, this assumes $d = 0$ and $\alpha_1 = \alpha_2 = 0$.

2. Direct input of the parameters a, b, c_i, d_i, δ_i, α_1, and α_2.

3. Input Skyrme parameters x_j and t_j ($j \in \{0, 1, 2, 3i\}$), and σ_i, which are used to determine a, b, c_i, d_i, δ_i, α_1, and α_2 as shown in Equations (14).

The last method has advantages over the first two. First, specifying only a few known nuclear experimental values to obtain the Skyrme coefficients (as in L&S) is unlikely to correctly predict other well determined physical constraints. Also, direct input of the parameters a, b, c_i, d_i, δ_i, α_1, and α_2 does not uniquely define the surface properties of nuclear matter for a Skyrme parametrization, specifically the parameters λ, q, and α discussed in Section II B. On the other hand, input of the Skyrme parameters x_j, t_j, and σ_i makes it straightforward to determine the surface properties of finite nuclei and to calculate nuclear matter properties that can be directly compared with experiments. Finally, most studies on Skyrme parametrizations in the literature explicitly give x_j, t_j, and σ_i.

For completeness, we give the expressions for the bulk specific entropy s_B, bulk specific free energy f_B, and bulk pressure P_B [3, 60]:

$$s_B = \frac{1}{n} \sum_t \left(\frac{5\hbar^2 \tau_t}{6 m_t^* T} - n_t \eta_t \right), \tag{15}$$

$$f_B = \epsilon_B / n - T s_B \,, \tag{16}$$

$$P_B = \sum_t n_t \mu_t - n f_B \,. \tag{17}$$

B. Nuclear surface

For a given density n, proton fraction y, and temperature T, nuclear matter may be uniform or phase separate into dense and dilute phases that are in thermal equilibrium. If the latter is the case, there will be some energy stored in the surface between the two phases. L&S parametrize the nuclear surface free-energy density F_S in terms of a surface shape function $s(u)$, a generalized nuclear size r, and the surface tension per unit area $\sigma(y_i, T)$, which is a function of the proton fraction y_i in the dense phase and temperature T. The surface free energy density is written as [3, 38]

$$F_S = \frac{3 s(u)}{r} \sigma(y_i, T) \,. \tag{18}$$

Both the generalized nuclear size r and the surface shape function $s(u)$ depend on the geometry of the heavy nuclei formed. While at low densities nuclei are spherical, as density increases and approaches nuclear saturation density, nuclei may assume shapes such as cylinders (think of pasta), slabs, cylindrical holes, and bubbles (think of Swiss cheese) [4, 5], as well as more exotic shapes [61–63]. In this picture, the generalized nuclear size r represents the radius of spherical nuclei or bubbles, the radius of cylinders or cylindrical holes, or the thickness of slabs. It is unclear what r should be for more exotic shapes. Following L&S, we do not consider specific geometries for the heavy nuclei and simply determine r by solving the nuclear virial theorem, see Equation (30) and the discussion in Section II C. The surface shape function $s(u)$, meanwhile, is chosen as an interpolating function that reproduces the low and high density limits for the shape of nuclei, which are, respectively, spheres ($\lim_{u\to 0} s(u) = u$) and bubbles ($\lim_{u\to 1} s(u) = 1 - u$). The simplest choice for this function is $s(u) = u(1-u)$, which is what L&S use[4] and we adopt here.

Following the prescription of [35, 38], the surface tension per unit area, $\sigma(y_i, T)$, is fitted by

$$\sigma(y_i, T) = \sigma_s h\left(y_i, T\right) \frac{2 \cdot 2^\lambda + q}{y_i^{-\lambda} + q + (1 - y_i)^{-\lambda}}, \tag{19}$$

where $\sigma_s \equiv \sigma(0.5, 0)$. The function $h(y_i, T)$ contains the temperature dependence in the form

$$h\left(y_i, T\right) = \begin{cases} [1 - (T/T_c(y_i))^2]^p \,, & \text{if } T \leq T_c(y_i) \,; \\ 0 \,, & \text{otherwise} \quad . \end{cases} \tag{20}$$

In Equations (19) and (20), λ, q, and p are parameters to be determined (see below), while $T_c(y_i)$ is the critical temperature for which the dense and the dilute phases coexist. The dense phase is assumed to have density n_i and proton fraction y_i while the dilute phase has density $n_o \leq n_i$ and proton fraction y_o.

To obtain the parameters λ, q, and p and a functional form for $T_c(y_i)$, we follow [35, 38, 59] and study the two phase equilibrium of bulk nucleonic matter. For a given proton fraction y, there exists a critical temperature T_c and a critical density n_c in which both the dense and dilute phases have the same density $n_i = n_o$ and same proton fraction $y_i = y_o$

[4] Note that this choice is not obvious in L&S's paper. It is, however, what is implemented in their source code.

(cf. Figures (2.3) and (2.4) of [38]). The quantities n_c and T_c are obtained by simultaneously solving [38]

$$\left.\frac{\partial P_B}{\partial n}\right|_T = 0 \qquad \text{and} \qquad \left.\frac{\partial^2 P_B}{\partial n^2}\right|_T = 0\,, \tag{21}$$

for proton fractions $y \leq 0.50$. Here, P_B is the bulk pressure given by Equation (17). Because we ignore Coulomb contributions to the surface tension, the formalism presented in this Section is almost symmetric under a $y \to 1-y$ transformation. The symmetry is only slightly broken by the small difference Δ in the neutron and proton rest masses, $m_n = m_p + \Delta$, which we ignore here when considering $y > 0.5$. Once the critical temperature T_c has been determined for a range of proton fractions y, we fit it using the function

$$T_c(y) = T_{c0}\left[a_c + b_c\delta(y)^2 + c_c\delta(y)^4 + d_c\delta(y)^6\right], \tag{22}$$

where $T_{c0} \equiv T_c(y=0.5)$ is the critical temperature for symmetric nuclear matter and $\delta(y) = 1-2y$ is the neutron excess.

After determining $T_c(y)$, we compute the properties of semi-infinite nucleonic matter, that is, matter for which the density varies along one direction (the z axis) and is constant in the remaining two. Ignoring Coulomb effects, we assume that in the limits $z \to \pm\infty$ matter saturates at densities n_i and n_o and proton fractions y_i and y_o. These two phases are in equilibrium if their pressures as well as their neutron and proton chemical potentials are the same, *i.e.*,

$$P_i = P_o\,, \quad \mu_{ni} = \mu_{no}\,, \quad \text{and} \quad \mu_{pi} = \mu_{po}\,. \tag{23}$$

Equations (23) are solved simultaneously with

$$y_i = \frac{n_{pi}}{n_{ni}+n_{pi}} \tag{24}$$

to obtain the neutron and proton densities of the high and low density phases n_{ni}, n_{pi}, n_{no}, and n_{po}, respectively.

Once the neutron and proton densities of the two coexisting phases have been calculated, we determine the surface shape that minimizes $\sigma(y_i,T)$. Since we assume the system to be homogeneous across two dimensions, the surface tension per unit area is given by [59, 64]

$$\sigma(y_i,T) = \int_{-\infty}^{+\infty}\Big[F_B(z) + E_S(z) + P_o - \mu_{no}n_n(z) - \mu_{po}n_p(z)\Big]dz\,. \tag{25}$$

Here, P_o, μ_{no}, and μ_{po} or, alternatively, P_i, μ_{ni}, and μ_{pi} are solutions to Equations (23). Meanwhile, $F_B(z) = n(z)f_B(n(z),y(z),T)$ is the bulk free energy density across the z axis, while $E_S(z)$ is the spatially-varying contribution to the energy density of a Skyrme-like Hamiltonian (see Equations 1–4 of Steiner *et al.* [59]). It has the form [35, 59, 64]

$$E_S(z) = \frac{1}{2}\Big[q_{nn}\left(\boldsymbol{\nabla}n_n\right)^2 + q_{np}\boldsymbol{\nabla}n_n\cdot\boldsymbol{\nabla}n_p + q_{pn}\boldsymbol{\nabla}n_p\cdot\boldsymbol{\nabla}n_n + q_{pp}\left(\boldsymbol{\nabla}n_p\right)^2\Big]\,, \tag{26}$$

where $n_t \equiv n_t(z)$ ($t \in \{n,p\}$). The parameters $q_{tt'}$ are related to the Skyrme coefficients by

$$q_{nn} = q_{pp} = \frac{3}{16}\left[t_1(1-x_1) - t_2(1+x_2)\right]\,, \tag{27a}$$

$$q_{np} = q_{pn} = \frac{1}{16}\left[3t_1(2+x_1) - t_2(2+x_2)\right]\,. \tag{27b}$$

As Steiner *et al.* point out [59], for Skyrme-type forces, the $q_{tt'}$ are constants and the relations $q_{nn} = q_{pp}$ and $q_{np} = q_{pn}$ are always true. In the general case, however, $q_{tt'}$ may be density dependent and q_{nn} may be different from q_{pp}, though $q_{np} = q_{pn}$ is still expected to hold.

To minimize Equation (25), we assume that the neutron and proton densities have a Woods-Saxon form, *i.e.*,

$$n_t(z) = n_{to} + \frac{n_{ti}-n_{to}}{1+\exp\left((z-z_t)/a_t\right)}\,, \tag{28}$$

where z_n and a_n (z_p and a_p) are, respectively, the neutron (proton) half-density radius and its diffuseness [65]. This form has the expected limits $\lim_{z\to-\infty} n_t(z) = n_{ti}$ and $\lim_{z\to+\infty} n_t(z) = n_{to}$. Following References [35, 59, 64], we set the proton half-density radius z_p at $z=0$ and minimize the surface tension per unit area with respect to the three other variables z_n, a_n, and a_p. This allows us to tabulate values of the surface tension per unit area $\sigma(y_i,T)$ as a function of the proton fraction y_i of the dense phase and the temperature T of the semi-infinite system. This is used to determine the parameters α and q in Equation (19) and p in Equation (20) performing a least squares fit.

It is worth mentioning that the surface free energy density should, in general, include a contribution from the neutron skin $\sigma \to \sigma + \mu_n\nu_n$, where ν_n is the neutron excess [38, 64]. However, we follow L&S, and neglect this term. In future work, this term should be included since its effects are important for very neutron rich matter [38].

C. Coulomb energy

Following L&S, we approximate the Coulomb free energy density using the static Wigner-Seitz approximation,

$$F_C = \frac{4\pi\alpha_C}{5}(y_i n_i r)^2 c(u)\,. \tag{29}$$

Here α_C is the fine structure constant, y_i is the proton fraction inside heavy nuclei, n_i the nuclear density also inside heavy nuclei, r is the generalized nuclear size, and $c(u)$ is the Coulomb shape function, discussed below.

In this model, only the surface and Coulomb energy densities depend on the generalized nuclear size r. Thus, minimizing the total energy density with respect to the nuclear size r implies that $F_S = 2F_C$, known as the nuclear virial theorem. With this, the generalized nuclear size becomes

$$r = \frac{9\sigma}{2\beta}\left[\frac{s(u)}{c(u)}\right]^{1/3}\,, \tag{30}$$

where

$$\beta = 9\left[\frac{\pi\alpha_C}{15}\right]^{1/3}(y_i n_i \sigma)^{2/3}\,, \tag{31}$$

and $\sigma \equiv \sigma(y_i, T)$ is the surface tension per unit area discussed in Section II B. Using the results of this section, the surface and Coulomb energy densities may be combined in the form

$$F_S + F_C = \beta\left[c(u)s(u)^2\right]^{1/3} \equiv \beta\mathcal{D}(u)\,. \tag{32}$$

This defines $\mathcal{D}(u)$ in terms of the surface and Coulomb shape functions, $s(u)$ and $c(u)$, respectively.

As is the case for the surface shape function $s(u)$ discussed in Section II B, the function $c(u)$ is also chosen to reproduce known physical limits [3, 38, 64]. At low densities, nuclei are spherical and the generalized nuclear size r is the nuclear radius. Considering the nuclei to occupy a small volume fraction of the Wigner-Seitz cell, $u \simeq 0$, the Coulomb shape function is given by $\lim_{u\to 0} c(u) = uD(u)$, where $D(u) = 1 - \frac{3}{2}u^{1/3} + \frac{1}{2}u$ [32]. Just below nuclear saturation density, $u \simeq 1$ and nuclei turn "inside out" and low-density spherical bubbles form inside an otherwise dense nucleonic phase. Here, the generalized nuclear size r is the bubble radius and $\lim_{u\to 1} c(u) = (1-u)D(1-u)$ [32]. Between these two limits matter may be more stable assuming non-spherical shapes, such as cylindrical and planar geometries [4, 5]. Using the results of Ravenhall *et al.* [4] for the structures that minimize the energy density of nucleonic matter with non-spherical geometries at zero temperatures, L&S showed that the function $\mathcal{D}(u)$ is well approximated by

$$\mathcal{D}(u) = u(1-u)\frac{(1-u)D(u)^{1/3} + uD(1-u)^{1/3}}{u^2 + (1-u)^2 + 0.6u^2(1-u)^2}\,, \tag{33}$$

again with $D(u) = 1 - \frac{3}{2}u^{1/3} + \frac{1}{2}u$. For simplicity, we make the same choice in our implementation.

D. Translational energy

Assuming that the heavy nuclei form a non-degenerate and non-relativistic Boltzmann gas with no internal degrees of freedom that is free to move within a Wigner-Seitz cell, we have [38]

$$F_T = \frac{u(1-u)n_i}{\bar{A}}h(y_i, T)\left(\mu_T - T\right)\,, \tag{34}$$

where

$$\mu_T = T\log\left(\frac{u(1-u)n_i}{n_Q\bar{A}^{5/2}}\right) \tag{35}$$

is the chemical potential of heavy nuclei with $n_Q = (m_n T/2\pi\hbar^2)^{3/2}$. Here

$$\bar{A} = \frac{4\pi n_i r^3}{3} \tag{36}$$

is the mass number of the representative heavy nucleus. One difference between our treatment and L&S is that they choose to set a fixed value for $\bar{A} = 60$ in the translational energy calculation. We, on the other hand, compute the value of the heavy nucleus mass number $\bar{A}$ and the translational energy F_T self-consistently. In order to guarantee that the translational free energy F_T also vanishes at the critical temperature $T_c(y_i)$, as is the case for the surface tension, we set F_T to be proportional to the function $h(y_i, T)$ [35] (see Equation 20).

Also, note that the heavy nuclei of course have internal degrees of freedom. These are accounted for in F_i (see Section II A).

III. SOLVING THE EOS

The model free energy described in Section II depends upon the variables u, r, n_i, y_i, n_{no}, n_{po}, n_α, and T. In thermodynamic equilibrium, the system will assume a state in which the free energy is minimized with respect to these variables, subject to the constraints of fixed baryon density, proton fraction, and temperature.

Our procedure is to search for extrema in the free energy surface, which is done by setting the derivatives of the free energy to zero and using standard root finding algorithms to find solutions to the resulting system of equations. First, we reduce the number of variables by using Equations (1) to express n_{no} and n_{po} in terms of the other variables and automatically obey baryon number and charge conservation. We then carry out minimization with respect to five independent variables: r, n_i, y_i, u, and n_α. Minimization with respect to r results in the constraint given by Equation (30). Setting the derivative of F with respect to n_α equal to zero gives

$$\mu_\alpha = 2(\mu_{no} + \mu_{po}) + B_\alpha - P_o v_\alpha\,, \tag{37}$$

which is just a condition for alpha particles in chemical equilibrium with the exterior protons and neutrons with an excluded volume correction. The derivatives with respect to the interior densities and the volume fraction give the constraints

$$A_1 = P_i - B_1 - P_o - P_\alpha = 0\,, \tag{38a}$$
$$A_2 = \mu_{ni} - B_2 - \mu_{no} = 0\,, \tag{38b}$$
$$A_3 = \mu_{pi} - B_3 - \mu_{po} = 0\,. \tag{38c}$$

In Equations (38), we use the quantities

$$B_1 = \frac{\partial\hat{F}}{\partial u} - \frac{n_i}{u}\frac{\hat{F}}{\partial n_i}\,, \tag{39a}$$
$$B_2 = \frac{1}{u}\left[\frac{y_i}{n_i}\frac{\partial\hat{F}}{\partial y_i} - \frac{\partial\hat{F}}{\partial n_i}\right]\,, \tag{39b}$$
$$B_3 = -\frac{1}{u}\left[\frac{1-y_i}{n_i}\frac{\partial\hat{F}}{\partial y_i} + \frac{\partial\hat{F}}{\partial n_i}\right]\,, \tag{39c}$$

where $\hat{F} = F_S + F_C + F_T$. The derivatives of F_S, F_C, and F_T with respect to the variables u, n_i, and y_i are readily obtained

from Equations (18), (29), and (34), respectively. This system of equations can then be solved to find the equilibrium values of the independent variables for fixed n, y, and T. These, in turn, can be used to calculate the pressure, entropy, and other thermodynamic quanties required by simulation codes.

We solve this system of non-linear equations by first using Equations (30) and (37) to explicitly find n_α and r. We then search for solutions to the three remaining contstraint equations using the independent variables $\zeta = [\log_{10}(u), \log_{10}(n_{no}), \log_{10}(n_{po})]$ and the root finding routines provided by [66]. Solving the system of equations requires initial guesses for the independent variables ζ. Often, an initial choice of ζ may not result in convergence of the root finding algorithm. Therefore, we perform an extensive search of possible initial guesses when the root finding algorithm fails, which allows us to gain convergence over a wider range of thermodynamic conditions than the original implementation of L&S. Since we are building tables, rather than using the EOS code directly in simulations, the increased computational expense is not burdensome.

In some regions of parameter space, uniform matter has a lower free energy than the non-uniform phase and is therefore the favored state. In uniform matter, $u = 0$ and the free energy has to be minimized with respect to n_{no}, n_{po}, and n_α, since the portion of the free energy that depends on r, n_i, and y_i is multiplied by u. Therefore, the properties of uniform matter can be found by solving Equation (37) subject to the neutron and proton number conservation constraints.

A significant difference between our EOS and that of L&S is our treatment of the transition between uniform and non-uniform mattter. L&S assume a continuous transition between uniform and non-uniform matter that is obtained using a Maxwell construction. In this picture, two phases with densities n_h and n_l, where $n_h > n_l$, are in thermal and chemical equilibrium with each other. The uniform higher density phase occupies a volume fraction $v = (n - n_l)/(n_h - n_l)$ of the system, while the non-uniform lower density phase occupies a volume fraction $(1-v)$. Hence, the free energy density in the boundary between both phases is

$$F(n, n_l, n_h, y, T) = vF_h(n_h, y, T) + (1 - v)F_l(n_l, y, T)\,, \tag{40}$$

and the equilibrium conditions used to obtain n_h and n_l are

$$\left.\frac{\partial F}{\partial n_l}\right|_{n_h,n,y,T} = \left.\frac{\partial F}{\partial n_h}\right|_{n_l,n,y,T} = 0\,. \tag{41}$$

Instead of using the L&S procedure, we determine what type of solutions may exist (uniform, non-uniform, or both) and solve the necessary system of equations. If only one of the systems has a physical solution then that is assumed to be the most stable configuration of nuclear matter. If both systems have solutions we choose the one with the lowest free energy as the favorable solution. This assumes that the transition from uniform to non-uniform matter is first order and, therefore, there is no coexistent phase as assumed by L&S and no need for a Maxwell construction.

We note that there are rare cases where non-uniform matter has lower free energy density than uniform matter, but we still set the latter as the favorable configuration. We make this choice whenever the adiabatic index

$$\Gamma = \left.\frac{\mathrm{d}\log P}{\mathrm{d}\log n}\right|_s \tag{42}$$

of non-uniform matter is negative, implying an unphysical imaginary speed of sound. This occurs rarely and typically at intermediate proton fraction $y \sim 0.20$ to 0.35, high density $n \sim 0.08$ to $0.11\,\mathrm{fm}^{-3}$, and low temperatures $T \lesssim 0.5\,\mathrm{MeV}$. In these cases, uniform and non-uniform matter have very similar free-energy densities and, therefore, we do not expect that choosing the phase with slightly higher free energy density will affect the EOS significantly.

IV. THE EQUATIONS OF STATE

The model and approach described in the previous sections can be used to compute thermodynamically consistent EOSs for a wide range of Skyrme parametrizations. There are over 200 Skyrme parametrizations in the literature. We focus on eight parametrizations that are able to reproduce most or all known experimental nuclear matter constraints according to Dutra *et al.* [9]. Since it has seen such wide use, we are also including the L&S EOS with $K_0 = 220\,\mathrm{MeV}$ although it does not fulfill many current nuclear physics constraints.

Specificially, we consider the following parametrizations (and provide EOS tables at https://stellarcollapse.org/SROEOS): NRAPR [59], SLy4 [73], SkT1 [71], SKRA [70], LNS [69], SQMC700 [74], Skxs20 [72], KDE0v1 [68], and L&S with $K_0 = 220\,\mathrm{MeV}$ (LS220 hereafter). Note that SLy4 does not fulfill one out of the eleven experimental constraints studied by Dutra *et al.*: its isospin incompressibility (Equation 52) is slightly below the experimentally allowed range. We include it since its zero-temperature variant has seen use in NS merger simulations (e.g., [75, 76]).

We summarize the Skyrme parameters t_i, x_i, and σ in Table I for the considered parametrizations. Note, however, that we exclude the L&S parametrization since there are multiple ways to set t_1, t_2, x_1 and x_2 that reproduce $\alpha_1 = \alpha_2 = 0$, see Equations (14f) and (14g). Furthermore, it is not straightforward to chose a combination of these four parameters that also reproduces the fit parameters for the surface tension per unit area $\sigma(y, T)$ used by L&S, see Equation (19) and Table III.

For completeness, we list the zero-temperature properties of uniform nuclear matter for all parametrizations in Table II. The included properties of symmetric nuclear matter (SNM) are the nuclear saturation density n_0, defined by

$$P = n^2 \left.\frac{\partial \epsilon_B(n, y)}{\partial n}\right|_{n=n_0, y=1/2} = 0\,, \tag{43}$$

the binding energy of SNM

$$\epsilon_0 = \epsilon_B(n_0, y = 1/2)\,, \tag{44}$$

TABLE I: Parameters of the considered Skyrme interactions with the exception of L&S, for which there are multiple ways to set t_1, t_2, x_1, and x_2 to achieve $\alpha_1 = \alpha_2 = 0$ in Equations (14f) and (14g). Here, t_0 is in $\mathrm{MeV\,fm^3}$, t_1 and t_2 are in $\mathrm{MeV\,fm^5}$, t_{31} is in $\mathrm{MeV\,fm^{3+3\sigma_1}}$, and x_0, x_1, x_2, x_{31}, and σ_1 are dimensionless. See References [9, 31, 67] for general discussions of these parameters.

Parametrization	t_0	t_1	t_2	t_{31}	x_0	x_1	x_2	x_{31}	σ_1
KDE0v1 [68]	−2553.08	411.69	−419.87	14063.61	0.6483	−0.3472	−0.9268	0.9475	0.1673
LNS [69]	−2484.97	266.735	−337.135	14588.2	0.06277	0.65845	−0.95382	−0.03413	0.16667
NRAPR [59]	−2719.70	417.64	−66.687	15042.0	0.16154	−0.047986	0.02717	0.13611	0.14416
SKRA [70]	−2895.4	405.5	−89.1	16660.0	0.08	0.0	0.2	0.0	0.1422
SkT1 [71]	−1794.0	298.0	−298.0	12812.0	0.154	−0.5	−0.5	0.089	0.33333
Skxs20 [72]	−2885.24	302.73	−323.42	18237.49	0.13746	−0.25548	−0.60744	0.05428	0.16667
SLy4 [73]	−2488.91	486.82	−546.39	13777.0	0.834	−0.344	−1.0	1.354	0.16667
SQMC700 [74]	−2429.10	370.97	−96.67	13773.42	0.10	0.0	0.0	0.0	0.16667

TABLE II: Properties of nuclear matter calculated for the considered Skyrme interactions. n_0 (in $\mathrm{fm^{-3}}$) is the saturation density of symmetric nuclear matter (SNM) and ϵ_0 (in $\mathrm{MeV\,baryon^{-1}}$) is the binding energy of SNM at n_0. Given in $\mathrm{MeV\,baryon^{-1}}$ are the incompressibility K_0, the skewness K', the symmetry energy parameters J, L, $K_{\rm sym}$, and $Q_{\rm sym}$, and the volume part of the isospin incompressibility $K_{\tau,v}$. $M_n^\star/m_n$ is the dimensionless ratio of the neutron effective mass to the neutron rest mass in SNM at n_0 and ΔM^* (in MeV) is the proton–neutron effective mass difference in SNM at n_0. Also given in MeV is the critical temperature T_c for two-phase coexistence. Small deviations between the LS220 results listed here and the original results of L&S are due to differences in the employed proton masses, the inclusion of the neutron proton mass difference (see the discussion in Section IV A) and from calculating the symmetry energy expansion parameters explicitly from the derivatives of ϵ_B and not from the difference in ϵ_B between SNM and pure neutron matter.

Parametrization	n_0	ϵ_0	K_0	K'	J	L	$K_{\rm sym}$	$Q_{\rm sym}$	$K_{\tau,\nu}$	M_n^*/m_n	ΔM^*	T_c
LS220 [3]	0.1549	−16.64	219.85	410.80	28.61	73.81	−24.04	96.17	−328.97	1.000	1.2933	16.80
KDE0v1 [68]	0.1646	−16.88	227.53	384.83	34.58	54.70	−127.12	484.44	−362.79	0.744	0.7166	14.85
LNS [69]	0.1746	−15.96	210.76	382.50	33.43	61.45	−127.35	302.52	−384.45	0.826	0.8821	14.92
NRAPR [59]	0.1606	−16.50	225.64	362.51	32.78	59.64	−123.32	311.60	−385.32	0.694	0.6224	14.39
SKRA [70]	0.1594	−16.43	216.97	378.73	31.32	53.04	−139.28	310.83	−364.92	0.748	0.7243	14.35
SkT1 [71]	0.1610	−16.63	236.14	383.49	32.02	56.18	−134.83	318.99	−380.68	1.000	1.2933	17.05
Skxs20 [72]	0.1617	−16.46	201.94	425.53	35.50	67.06	−122.31	328.52	−383.37	0.964	1.2015	15.37
SLy4 [73]	0.1595	−16.62	229.90	363.07	32.00	45.96	−119.70	521.48	−322.84	0.695	0.6241	14.52
SQMC700 [74]	0.1704	−16.14	219.59	367.98	33.40	59.14	−140.23	312.66	−395.42	0.755	0.7385	14.72

the effective mass of nucleons at saturation density for SNM, $M_t^* = m_t^*(n_0, y = 1/2)$, the incompressibility

$$K_0 = 9n_0^2(\partial^2\epsilon_B/\partial n^2)|_{n=n_0,y=1/2}\,, \tag{45}$$

and the skewness

$$K' = -27n_0^3(\partial^3\epsilon_B/\partial n^3)|_{n=n_0,y=1/2}\,. \tag{46}$$

Here, $\epsilon_B = E_B/n$ is the specific energy per baryon of uniform matter. These quantities define the expansion of the specific energy of SNM around saturation density,

$$\epsilon_B(n, y = 1/2) = \epsilon_0 + \frac{1}{2}K_0x^2 - \frac{1}{6}K'x^3 + \mathcal{O}(x^4)\,, \tag{47}$$

where $x = (n - n_0)/3n_0$ and, as in Equation (7), $\Delta = m_n - m_p$.

The specific energy per baryon of asymmetric nuclear matter may be expanded around its value for symmetric matter,

$$\epsilon_B(n, y) = \epsilon_B(n, y = 1/2) + \mathcal{S}(n)\delta(y)^2 + \mathcal{O}(\delta(y)^4)\,, \tag{48}$$

where $\delta(y) = 1 - 2y$ is the isospin asymmetry and $S(n)$ is the density-dependent symmetry energy, which is defined as

$$\mathcal{S}(n) = \frac{1}{8}\left.\frac{\partial^2\epsilon_B(n, y)}{\partial y^2}\right|_{n,y=1/2}\,. \tag{49}$$

Sometimes the symmetry energy is defined as $S(n) = \epsilon_B(n, 0) - \epsilon_B(n, 1/2)$. The two definitions agree up to their quadratic terms. We plot $\mathcal{S}(n)$ for the considered Skyrme parametrizations in Figure 1. We show curves for both uniform matter obtained from Equation (49) with $\epsilon_B(n, y)$ given by Equation (7), and for non-uniform matter, *i.e.*, accounting for the clustering of nucleons into heavy nuclei, which occurs for densities $n \lesssim 0.10\,\mathrm{fm^{-3}}$. For zero-temperature, non-uniform symmetric matter, the only non-negligible density-dependent contribution comes from the term $F_i = u_i n_i f_B(n, y)$, which to first order is approximated by the binding energy of symmetric nuclear matter $n_0 f_B(n_0, 1/2)$. At high densities, $n \gtrsim 3n_0$, nuclear physics observables are poorly constrained and the behavior of $\mathcal{S}(n)$, obtained as an expansion about n_0, is highly uncertain.

Expanding $\mathcal{S}(n)$ as a function of x, one obtains

$$\mathcal{S}(n) = J + Lx + \frac{1}{2}K_{\rm sym}x^2 + \frac{1}{6}Q_{\rm sym}x^3 + \mathcal{O}(x^4)\,, \tag{50}$$

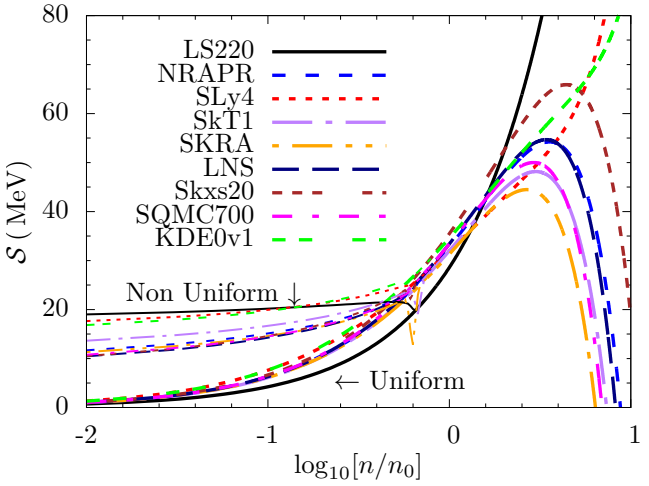

FIG. 1: (Color online) Density dependence of the symmetry energy $\mathcal{S}(n)$ for all considered Skyrme parametrizations. The thick curves show $\mathcal{S}(n)$ for uniform nuclear matter (neutrons and protons only) obtained from Equation (49) with $\epsilon_B(n, y)$ given by Equation (7). The thin curves correspond to $\mathcal{S}(n)$ for the full high-density EOS at zero temperature, allowing for non-uniform and uniform nuclear matter. At densities below the transition to uniform matter, $\mathcal{S}(n)$ is obtained from Equation (49) with $\epsilon_B(n, y)$ replaced by F/n with F from Equation (2). Note that the high density ($n \gg n_0$) behavior of $\mathcal{S}(n)$ is highly uncertain. The high-density shape of $\mathcal{S}(n)$ for the Skyrme parametrizations shown here is a mere artifact of the expansion about n_0 and is not necessarily physical. At low density, the binding energy of nearly symmetric nuclei increases the value of the symmetry energy for non-uniform matter.

where

$$J = \mathcal{S}(n_0)\,, \tag{51a}$$
$$L = 3n_0(\partial\mathcal{S}/\partial n)|_{n=n_0}\,, \tag{51b}$$
$$K_{\rm sym} = 9n_0^2(\partial^2\mathcal{S}/\partial n^2)|_{n=n_0}\,, \tag{51c}$$
$$Q_{\rm sym} = 27n_0^3(\partial^3\mathcal{S}/\partial n^3)|_{n=n_0}\,. \tag{51d}$$

These expansion parameters are listed in Table II. We note that the symmetry energy parameters J and L for all of the Skyrme parametrizations, except for LS220, are consistent with recently conjectured unitary gas constraints [17].

We also show in Table II the volume part of the isospin incompressibility $K_{\tau,v}$ (e.g., [9]), given by

$$K_{\tau,v} = \left(K_{\rm sym} - 6L - \frac{Q_0}{K_0}L\right), \tag{52}$$

the effective mass of neutrons in SNM M_n^*, the neutron proton effective mass difference in SNM, $\Delta M^* = M_n^* - M_p^*$, and the critical temperature T_0 discussed in Section II B. Note that most parametrizations have $T_c \simeq 15\,\text{MeV}$, the exceptions being the SkT1 and LS220 parametrizations that have slightly higher critical temperatures, $T_c \simeq 17\,\text{MeV}$, which is due to their high effective masses. For completeness, we provide the coefficients obtained for the critical temperature expansion (Equation 22) in Appendix C.

TABLE III: Summary of the surface properties of nuclear matter obtained for the considered Skyrme parameterizations. S_S is the surface symmetry energy (in MeV; Equation 53a), A_S is the surface level density (in MeV^{-1}; Equation 53b), σ_s is the surface tension of symmetric nuclear matter at zero temperature (in MeV fm^{-2}; Equation 25). q, λ, and p are the dimensionless surface tension parameters in Equations (19) and (20).

Parametrization	S_S	A_S	σ_s	q	λ	p
LS220 [3]	45.81	0.1365	1.150	24.40	3.000	2.000
KDE0v1 [68]	78.63	0.1315	1.215	13.54	3.245	1.493
LNS [69]	95.17	0.1089	1.044	7.78	3.507	1.506
NRAPR [59]	92.44	0.1316	1.140	13.96	3.522	1.467
SKRA [70]	86.99	0.1332	1.125	14.26	3.464	1.492
SkT1 [71]	78.71	0.0979	1.090	16.06	3.449	1.606
Skxs20 [72]	106.94	0.1117	1.045	6.48	3.540	1.555
SLy4 [73]	64.31	0.1423	1.247	18.51	3.128	1.474
SQMC700 [74]	98.48	0.1280	1.191	9.90	3.442	1.486

In Table III, we list the parameters σ_s, q, λ, and p that determine the surface tension per unit area, and which we obtain as described in Section II B. We also provide the values of the surface symmetry energy parameter S_S and the surface level density parameter A_S given by

$$S_S = -\frac{A^{1/3}}{8}\left(\frac{\partial^2 f_S(y,T)}{\partial y^2}\right)\Bigg|_{y=1/2,T=0}\,, \tag{53a}$$
$$A_S = -\frac{A^{1/3}}{2}\left(\frac{\partial^2 f_S(y,T)}{\partial T^2}\right)\Bigg|_{y=1/2,T=0}\,, \tag{53b}$$

where f_S is calculated for a spherical nucleus with mass number A and density n_0, *i.e.*,

$$f_S(y,T) = \frac{4\pi r_N^2\sigma(y,T)}{A}\,, \tag{54}$$

with $r_N = (3/4\pi n_0 A)^{1/3}$. Compared with the LS220 parametrization, all other Skyrme parametrizations have a much higher surface symmetry energy parameter S_S, lower values for the parameters q and p, and a higher value for λ. In Reference [38], Lim and Lattimer argue that the exponent λ is expected to be between 2 and 4. This result agrees with our results, though we find the range of λ to be smaller for all considered parametrizations, namely $3 \lesssim \lambda \lesssim 3.5$. Finally, there are significant differences between the surface properties we derive here for the SLy4 and those provided by Lim and Lattimer [38]. The differences reside in Lim and Lattimer having an extra parameter that accounts for the surface tension of the neutron skin of nuclei, $\sigma \to \sigma + \mu_n\nu_n$, as discussed in Section II B.

A. Comparison with L&S results

Using the same L&S Skyrme parametrization which predicts a nuclear incompressibility $K_0 = 220\,\text{MeV}$, we compare the results from our code, labeled here as LS220†,

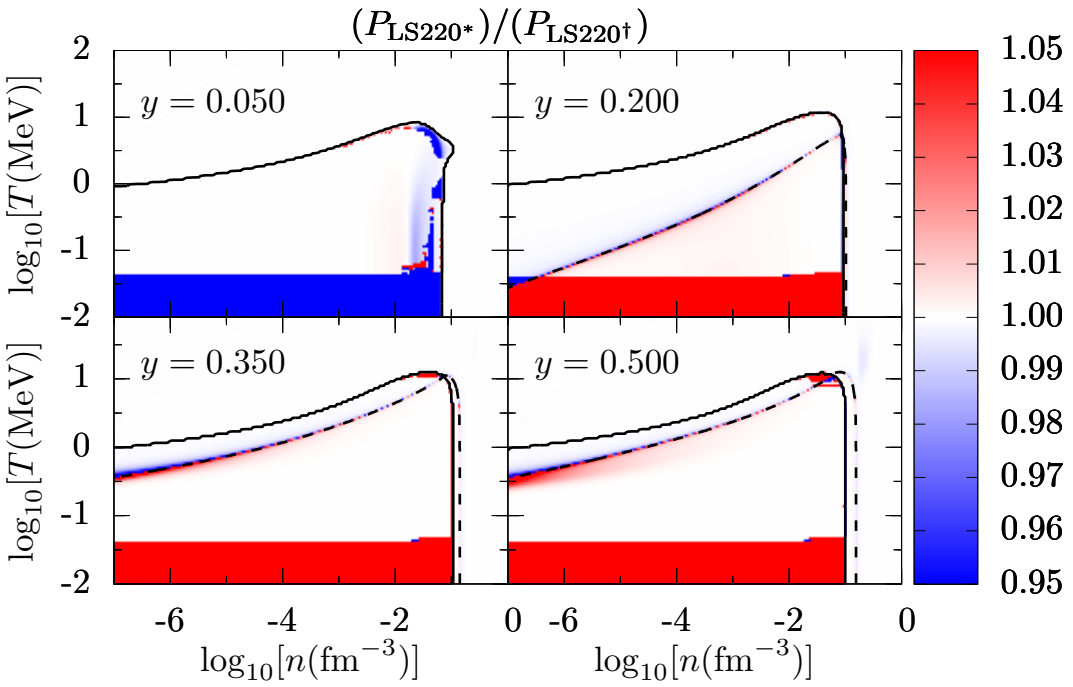

FIG. 2: (Color online) Comparison with L&S . We show the ratio of nuclear pressure for a range of proton fractions obtained with our LS220† implementation and with the original L&S implementation LS220*. The solid black curve deliniates where the heavy-nuclei number fraction $X_i = un_i/n$ changes from zero to a non-zero value. Below and to the left of the curve, matter is non-uniform, while above and to the right of the line it is uniform. The dashed line shows where the nuclear pressure is zero. Differences between LS220† and LS220* are largest near this line. The wide horizontal band at the bottom of the panels marks the region where the original L&S implementation does not converge for non-uniform nuclear matter and assumes that the system is uniform.

with the results of the original L&S implementation available at http://www.astro.sunysb.edu/dswesty/lseos.html, labeled here as LS220*. In order to be consistent in our comparison with the original L&S implementation, for the cases discussed in this subsection only, we make the following choices: (1) We set the alpha-particle binding energy to $B_\alpha = 28.3\,{\rm MeV}$. (2) We set $m_p = m_n = 939.5654\,{\rm MeV}$. (3) We set the proton-neutron mass difference to $\Delta = 1.29\,{\rm MeV}$ and carry it explicitly. (4) We fix $\bar{A} = 60$ in Equation (36).

In Figure 2, we plot the ratio of the total nuclear pressures (excluding electrons and photons) returned by the two LS220 implementations. We choose proton fractions of $y = 0.05$, 0.20, 0.35, and 0.50, densities in the range $10^{-7}\,{\rm fm}^{-3} \leq n \leq 1\,{\rm fm}^{-3}$, and temperatures $0.01\,{\rm MeV} \leq T \leq 100\,{\rm MeV}$. We choose these ranges since the original L&S implementation only converges consistently for proton fractions in the range $0.03 \leq y \leq 0.51$, densities higher than $10^{-7}\,{\rm fm}^{-3}$, and temperatures higher than $10^{-1.5}\,{\rm MeV}$. In our implementation, however, we are able to compute the EOS for proton fractions $0.001 \lesssim y \lesssim 0.7$, and for temperatures and densities as low as $10^{-4}\,{\rm MeV}$ and $10^{-13}\,{\rm fm}^{-3}$, respectively.

Figure 2 demonstrates that in uniform matter, with the exception of regions very close to $P \simeq 0$, our results and those of L&S agree within 0.5% or better. For non-uniform matter and very low temperatures, $T \lesssim 0.04\,{\rm MeV}$, the L&S implementation is unable to find a non-uniform solution and assumes the system is uniform. This gives rise to the large ratio between the pressures in that region. In most of the non-uniform regions with temperatures above $T \gtrsim 0.04\,{\rm MeV}$, the agreement is, again, within 0.5% or better. Exceptions occur near the transition from uniform to non-uniform matter and regions where the nuclear pressure is close to zero. Even though the ratios are large in these regions, the absolute pressure differences are relatively small. Differences between the two implementations also appear in regions of parameter space with very low proton fraction, represented in Figure 2 by $y = 0.05$, and densities $0.006\,{\rm fm}^{-3} \lesssim n \lesssim 0.03\,{\rm fm}^{-3}$. Discrepancies are also visible in regions of non-uniform symmetric nuclear matter at temperatures $T \simeq 10\,{\rm MeV}$. In these regions, the original L&S implementation has convergence issues for some values of density n and temperature T. At very low proton fraction, even in regions where both implementations converge, we observe differences in the calculated pressures as large as 2%.

We carry out similar comparison studies for other thermodynamic quantities, including the specific energy, specific entropy, proton and neutron chemical potentials, average nuclear charge and mass, and the mass fractions of protons, neutrons, alpha particles, and heavy nuclei. In all these comparisons we find differences that are qualitatively and quantitatively very similar to what is shown for the pressure in Figure 2.

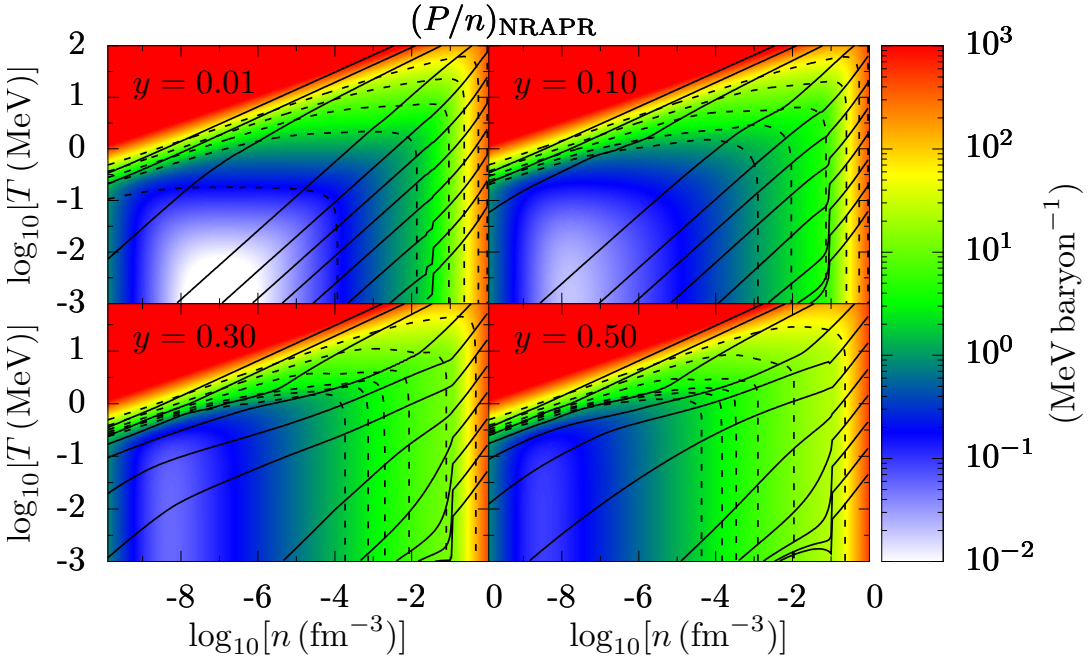

FIG. 3: (Color online) Total pressure per nucleon P/n in $\mathrm{MeV\ baryon}^{-1}$ for the NRAPR Skyrme parametrization [59] and proton fractions $y = 0.01, 0.10, 0.30$, and 0.50. The solid black curves denote, from top to bottom, the adiabats at entropies $s = 10^n k_B\,\mathrm{baryon}^{-1}$ for $n = 2$ to $n = -3$ in -0.5 increments. The dashed black curves correspond, from right to left, to the isoergs for specific energies $\epsilon = 100, 30, 10, 3, 0$, and $-3\,\mathrm{MeV\,baryon}^{-1}$. Note that only the $y = 0.30$ and $y = 0.50$ panels contain the $\epsilon = -3\,\mathrm{MeV\,baryon}^{-1}$ isoerg. The pressure per nucleon is dominated by electrons, positrons, and photons in large portions of the density–temperature space. Only at the highest densities, at and above saturation density, is the pressure dominated by the nucleon contributions and the impact of strong interactions.

B. Comparing Equations of State

We compare full EOSs obtained with the set of considered Skyrme parametrizations. We focus on SNA EOSs and defer a detailed discussion of our approach for matching to NSE at low densities to Section VII A. In contrast to the previous section on the LS220 parametrization, we go back to an alpha particle binding energy of $B_\alpha = 30.887\,\mathrm{MeV}$ since all free energies are computed with respect to the free energy of a gas of unbound neutrons. We set $m_p = 938.2721\,\mathrm{MeV}$ and $m_n = 939.5654\,\mathrm{MeV}$ [77]. The proton-neutron mass difference $\Delta = m_n - m_p$ is obtained self-consistently. Despite changing the proton mass, our LS220 implementation uses the same Skyrme parameters obtained by L&S and used in Section IV A. This results in small differences between the LS220 EOS and the LS220† and LS220* EOSs. The differences come from small changes in the proton effective mass term, Equation 8. Finally, we let $\bar{A}$ vary in the translational free energy density (Equation 36).

In Figure 3, we plot the pressure per nucleon using the NRAPR parametrization for proton fractions $y = 0.01, 0.10$ 0.30, and 0.50. We also include in the plots eleven adiabats, $s = 10^n k_B\,\mathrm{baryon}^{-1}$ for $n = -3$ to $n = 2$ in 0.5 increments, and six isoergs at $\epsilon = -3$, 0, 3, 10, 30, and $100\,\mathrm{MeV\,baryon}^{-1}$. The pressure per baryon is dominated by the electron and photon contributions in large portions of density–temperature space. At the highest temperatures, the electrons, positrons, and photons behave as an ultra-relativistic gas and drive the strong temperature dependence of the pressure seen there. At lower temperatures ($T \lesssim 1\,\mathrm{MeV}$) and for densities below saturation density, degenerate electrons give a large contribution to the pressure and the pressure is relatively insensitive to the temperature. Nevertheless, throughout the phase diagram, the nuclear contribution to the pressure is often significant, although subdominant. At the highest densities (i.e., at and above saturation density), the pressure is dominated by the nucleon contributions and the impact of strong interactions. The EOSs obtained from the other Skyrme parametrizations considered in this study are qualitatively similar to the EOS resulting from the NPAPR parametrization and shown in Figure 3.

In Figure 4, we plot the temperatures along four adiabats ($s = 0.01$, 0.1, 1, and $10\,k_B\,\mathrm{baryon}^{-1}$) at a range of proton fractions. Except for very low entropies, $s \lesssim 0.1\,k_B\,\mathrm{baryon}^{-1}$, or very high densities, $n \gtrsim 0.1\,\mathrm{fm}^{-3}$, the entropy does not significantly depend on the Skyrme parametrization. For uniform matter, the entropy depends only on the temperature, density, proton fraction, and nucleon effective masses. Therefore, we see systematically higher entropies for parametrizations with smaller effective masses at high density. At lower densities, variations between EOSs are caused by the different properties of the single nucleus predicted by the different Skyrme parametrizations.

In Figure 5, we compare the adiabatic index Γ, Equation (42), along the $s = 1\,k_b\,\mathrm{baryon}^{-1}$ adiabats. The largest dif-

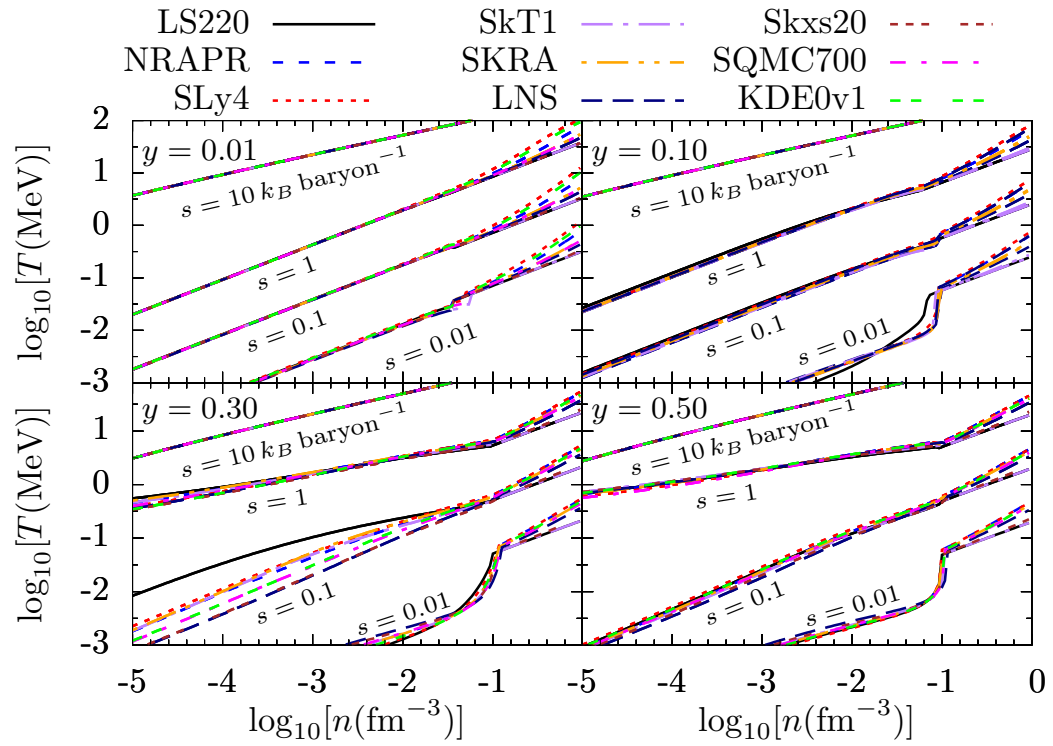

FIG. 4: (Color online) Temperature along adiabats with specific entropy $s = 10$, 1.0, 0.1, and $0.01\,k_B$ baryon^{-1} in the single-nucleus approximation and for all considered Skyrme parametrizations. Note that electrons, positrons, and photons are included. The adiabats differ mostly in regions dominated by nucleonic pressure around and above saturation density $n_0 \sim 0.16$ fm^{-3} and for $y \simeq 0.30$ and $T \lesssim 1$ MeV, where the number of free neutrons varies significantly between parametrizations.

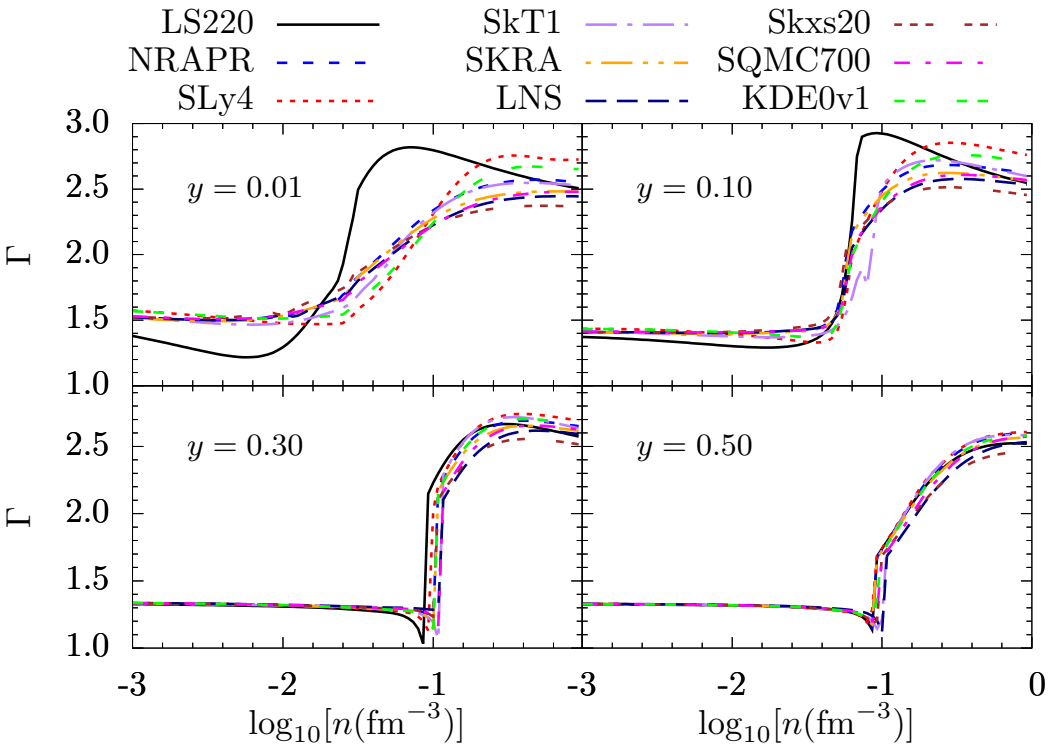

FIG. 5: (Color online) Adiabatic index Γ along the $s = 1\,k_B$ baryon^{-1} adiabat for full EOSs in the single-nucleus approximations. At low densities and proton fractions $y \gtrsim 0.1$, electrons dominate and $\Gamma \sim 4/3$. At high densities and $y = 0.50$, Γ is roughly the same for all EOSs reflecting the well constrained properties of symmetric nuclear matter. The sharp discontinuity is due to the transition between non-uniform and uniform nuclear matter at $n \simeq 0.1$ fm^{-3}. It becomes smoother at lower proton fraction due to large free neutron contributions. Also, as the proton fraction decreases, differences between parametrizations increase due largely to variations in the density-dependent symmetry energy (cf. Figure 1.)

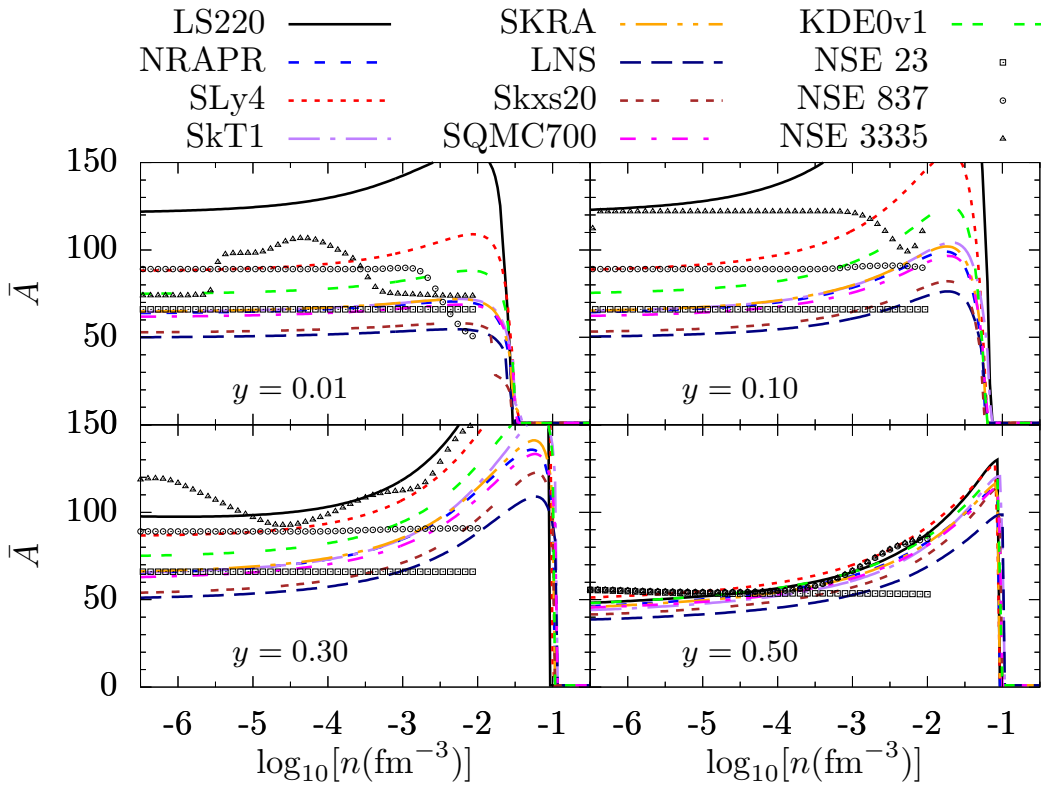

FIG. 6: (Color online) Average heavy nucleus mass number $\bar{A}$ along the $s = 1\,k_B\,\mathrm{baryon}^{-1}$ adiabat as a function of density for the considered Skyrme parametrizations in the single-nucleus approximation (SNA) and, at low densities, for nuclear-statistical equilibrium (NSE) with 23, 807, and 3 335 nuclides (we discuss our NSE treatment and matching to SNA in Section VII A). For the SNA curves, differences in nuclear sizes result from differences in symmetry energy and the surface properties obtained for each parametrization. The 3 335 nuclide NSE network exhibits large oscillations in $\bar{A}$. These are due to nuclear shell effects included implicitly in the nuclear masses.

ferences between the adiabatic indexes occur for very low proton fractions, $y \lesssim 0.10$. This follows from the Skyrme parameters being chosen to fit properties of isospin symmetric matter and, therefore, predicting significantly different properties of matter when extrapolated to large isospin asymmetries. In the very neutron rich regime, $y \lesssim 0.10$, the LS220 parametrization shows results that differ from the others not only quantitatively, but also qualitatively. Unlike the other parametrizations, at low proton fractions, Γ_{LS220} exhibits a peak close to the phase transition between non-uniform and uniform matter. The change of Γ_{LS220} across the transition is overall much smoother and occurs at lower densities than for the other parametrizations.

The composition of non-uniform matter influences the EOS and can impact neutrino transport in CCSNe. Each Skyrme parametrization predicts different properties for the equilibrium nucleus in the SNA. In Figure 6, we show the masses $\bar{A}$ of the SNA nuclei formed along the $s = 1\,k_B\,\mathrm{baryon}^{-1}$ adiabat for different Skyrme parametrizations. We compare them with $\bar{A}$ obtained for ensembles of nuclei in NSE (see Section VII A). The LS220 parametrization produces much heavier nuclei at low y than any of the other parametrizations. By Equation 30, the nuclear size r increases with the surface tension. Therefore, increasing σ increases $\bar{A}$, all other things being equal. LS220 has the weakest y dependence of the surface tension (which results in a relatively larger surface tension at low y) and the smallest symmetry energy of any of the Skyrme parameterizations. This explains the large nuclei predicted by LS220. The Skxs20 and LNS parametrizations predict the lightest nuclei and have the smallest surface tensions at low y. Except for some parametrizations at very low proton fractions, the SNA EOSs produce heavy nuclei that increase with density for $n \gtrsim 10^{-4}\,\mathrm{fm}^{-3}$ until close to the phase transition to uniform nuclear matter. This is the region where the nuclear "pasta" phase is expected to appear. The different masses of nuclei may significantly alter neutrino cross sections and CCSNe neutrino spectra as well as the cooling rates of NSs. Since Skyrme parametrizations are fitted to properties of SNM, all parametrizations yield similar predictions for $\bar{A}$ at $y = 0.5$.

Figure 6 includes NSE results for $\bar{A}$ that were obtained with ensembles of 23, 837, and 3 335 nuclides. We see that $\bar{A}$ predicted by NSE for the $s = 1\,k_B\,\mathrm{baryon}^{-1}$ adiabat is rather sensitive to the number of nuclides included. In the ensemble containing 23 nuclei, which includes nuclides with $Z \leq 26$, the only heavy and neutron rich nuclide included, ^{66}Fe, dominates the composition for neutron rich matter. The 837-nuclide ensemble includes nuclides with $Z \leq 50$ and the dominant nucleus for neutron rich matter is ^{89}Ge.

The 3 335-nuclide NSE network includes nuclides up to

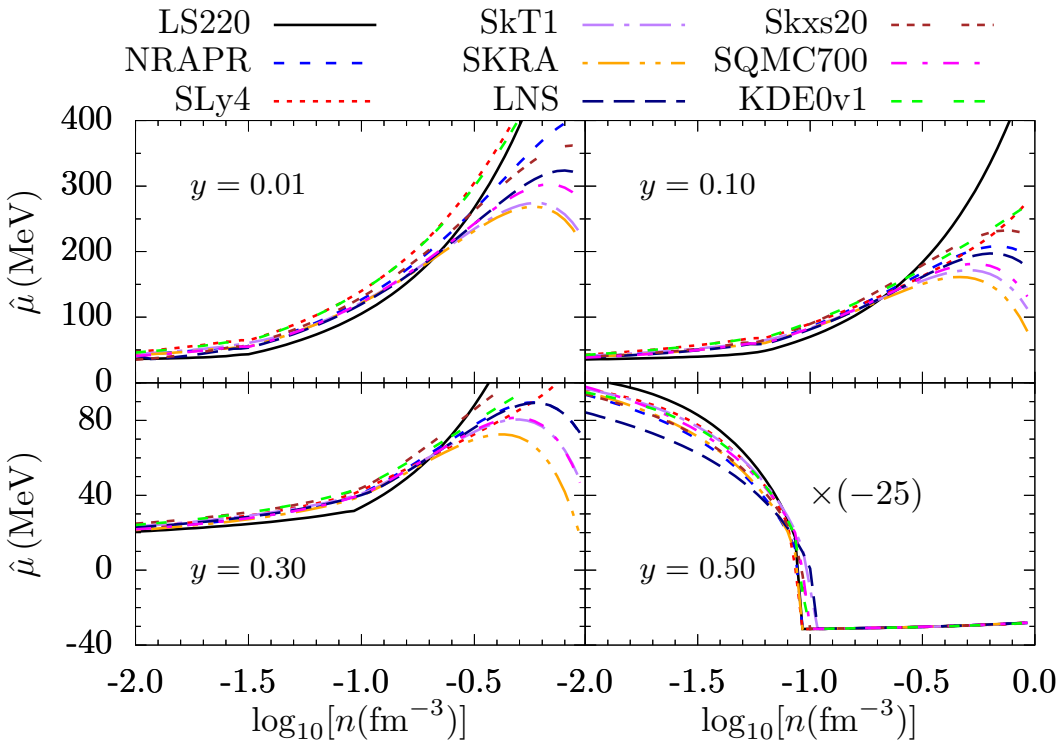

FIG. 7: (Color online) Neutron-proton chemical potential difference $\hat{\mu} = \mu_n - \mu_p$ along the $s = 1.0\,k_B$ baryon^{-1} adiabat as a function of density for the considered Skyrme parametrizations at proton fractions $y = 0.01$, 10, 0.30, and 0.50. Note that we multiply $\hat{\mu}$ by a factor of -25 in the bottom right panel showing the $y = 0.5$ case. $\hat{\mu}$ is sensitive to the density dependence of the symmetry energy and the differences between parametrizations seen here correlate with those in Figure 1.

$Z = 85$ and sufficiently many neutron-rich heavy nuclides that there is no single nuclide that dominates in neutron rich matter. For SNM, on the other hand, all nuclide ensembles predict very similar compositions at low densities, $n \lesssim 10^{-4}\,\mathrm{fm}^{-3}$.

Finally, we present in Figure 7 the difference between the neutron and proton chemical potentials, $\hat{\mu} = \mu_n - \mu_p$, along the $s = 1\,k_B$ baryon^{-1} adiabat. The quantity $\hat{\mu}$ is relevant for charged current neutrino interactions as it enters into the equilibrium neutrino chemical potential, $\mu_\nu = \mu_e - \hat{\mu}$, which determines detailed balance for charged current interactions and influences how hard it is to turn neutrons into protons (or vice versa) in the medium. Furthermore, $\hat{\mu}$ is correlated with the symmetry energy $\mathcal{S}$, which gives a large contribution to the pressure at high densities. First, we note that for SNM, all Skyrme parametrizations produce similar curves for $\hat{\mu}$, especially for densities $n \gtrsim 0.1\,\mathrm{fm}^{-3}$. This is expected, since the coefficients of each parametrization are chosen to reproduce properties of uniform SNM where experimental constraints are abundant.

It is apparent from Figure 7 that for most proton fractions the LS220 parametrization predicts the lowest values for $\hat{\mu}$ in the range $0.01\,\mathrm{fm}^{-3} \lesssim n \lesssim n_0$ and the highest for densities above nuclear saturation density. In the neutron rich regime, the LS220, SLy4, and KDE0v1 parametrizations all predict $\hat{\mu}$ that increases monotonically with density. The other parametrizations, on the other hand, have a global maximum above nuclear saturation density, which occurs in the range $2n_0 \lesssim n \lesssim 4n_0$ and is higher (lower) for Skxs20 (SKRA) than for the other parametrizations. In the next Section V, we discuss the effects of this behavior on the radial profile and maximum mass of cold nonrotating NSs.

V. NEUTRON STAR MASS-RADIUS RELATIONSHIP

We construct the mass-radius relationship of cold neutron stars (NS) by solving the Tolman-Oppenheimer-Volkoff (TOV) equations [78] for neutrino-less beta equilibrated matter (BEM) near zero temperature. We choose a low temperature of $T = 0.1\,\mathrm{MeV}$, and determine for each density n the proton fraction y where the neutrino chemical potential is zero, *i.e.*, $\mu_\nu = \mu_e - \mu_n + \mu_p = 0$. If no such solution can be found, or the solution implies a large discontinuity from $y \simeq 0$ to $y > 0.50$, we set the proton fraction to the minimum value available for a given combination of n and T in the EOS table.

In Figure 8, we present density-dependent graphs of pressure, specific internal energy, and proton fractions for the LS220, NRAPR, SLy4, LNS, and KDE0v1 parametrizations. For comparison, we also show results obtained with the orig-

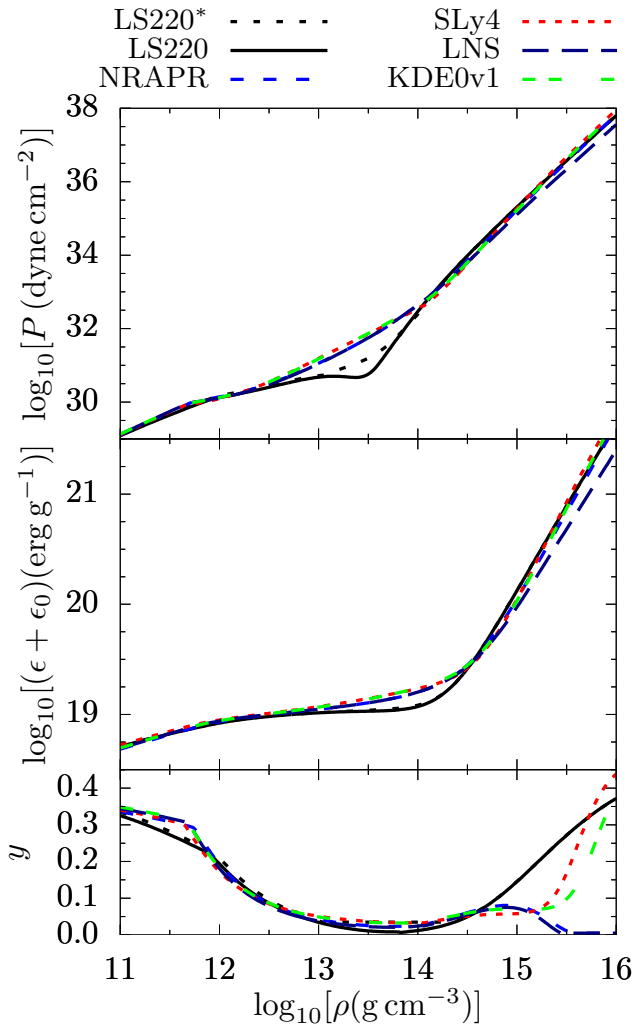

FIG. 8: (Color online) Pressure P (top panel), specific internal energy ϵ (plus an additive constant $\epsilon_0 = 2 \times 10^{19}\,\mathrm{erg\,g^{-1}}$; center panel), and proton fraction y for low temperature neutrino-less beta equilibrated matter (bottom panel). We show results for five select Skyrme parametrizations that span the range of maximum neutron star masses shown in Figure 9. The LS220* (LS220) curve uses L&S's (our) implementation of the L&S $K_0 = 220\,\mathrm{MeV}$ parametrization. Differences between LS220 and LS220* are due to the L&S implementation limit of proton fractions $y \geq 0.035$ and a small difference in the proton masses used (cf. Section IV A). The proton fraction y at high densities, $\rho \gtrsim 10^{14.5}\,\mathrm{g\,cm^{-3}}$, mirrors the high density behavior of the symmetry energy $\mathcal{S}(n)$ (cf. Figure 1).

inal L&S implementation (LS220*), which converges reliably only for proton fractions $y \gtrsim 0.035$.

Figure 8 reveals some differences between the LS220 and the LS220* curves. These are due to small differences in chemical potentials between the EOSs owing to the different treatments of proton masses (cf. Section IV A) and to the L&S implementation limit of proton fractions $y \geq 0.035$. The four other parametrizations shown in Figure 8, SLy4, KDE0v1, NRAPR, and LNS, have very similar qualitative and quantitative behavior below nuclear saturation density in the three quantities plotted. For densities above nuclear saturation density, on the other hand, the EOSs can be separated into two groups according to their prediction for the BEM proton fraction. Group I EOSs, which includes the LS220, LS220*, SLy4, and KDE0v1 parametrizations, have proton fractions that increase monotonically above nuclear saturation density. Meanwhile, Group II EOSs, which include the NRAPR and LNS parametrizations, have BEM proton fractions with a maximum near nuclear saturation density and that decrease to zero at higher densities. Group II also includes the other four parametrizations that we consider in this study (SKRA, SkT1, Skxs20, and SQMC700), but do not show in Figure 8.

The two different behaviors in the proton fraction above nuclear saturation density can be traced back to the symmetry energy $\mathcal{S}$ (shown in Figure 1) and the related neutron-proton chemical potential difference $\hat{\mu}$ (see Figure 7). The EOSs in Group I have $\mathcal{S}$ and $\hat{\mu}$ for neutron rich matter that increase monotonically with density. Therefore, above nuclear saturation density, their proton fraction y for BEM also increases monotonically with density. In Group II, meanwhile, both $\mathcal{S}$ and $\hat{\mu}$ have a maximum at a density above nuclear saturation and then decrease for higher densities. Figure 7 shows the density dependence of $\hat{\mu}$ for the $s = 1\,k_B\,\mathrm{baryon}^{-1}$ adiabat, which is qualitatively similar to the density dependence near zero temperature and entropy. In Reference [67], Stone *et al.* argued that a key quantity for distinguishing between these two groups of Skyrme parametrizations is the density dependence of the symmetry energy, expressed by the asymmetry parameter

$$a_s(n) = \epsilon_B(n, y = 1/2) - \epsilon_B(n, y = 0)\,. \qquad (55)$$

Stone *et al.* argued that parametrizations for which a_s and, thus, $\hat{\mu}$ increases monotonically with density above saturation density, are more realistic since their behavior matches that observed for realistic nuclear potentials. Realistic nuclear potentials, such as the Argonne v_{18} [80], CD-Bonn [81] and Nijmegen II [82] are obtained by fitting 40 to 60 adjustable parameters to thousands of experimental data points of free nucleon-nucleon scattering and properties of the deuteron.

In Figure 9, we show the NS mass-radius curves that we obtain by solving the TOV equations with our EOSs. We also indicate the mass of the currently most massive known NS (PSR J0348+0432 [79]) and the 2σ confidence region for the NS mass-radius relationship given by "model A" of Nätillä *et al.* [12]. They obtained these constraints via a Bayesian analysis of Type-I X-ray burst observations. For completeness, we summarize in Table IV key properties of the TOV NS sequences obtained with all considered Skyrme parametrizations.

We note from Figure 9 that there is a small difference between the mass-radius relation curves for NSs obtained with the LS220 and LS220* EOSs for low-mass NSs. Recall that LS220 represents results from our full SNA implementation of the LS220 parametrization and LS220* represents results obtained with an EOS table generated with the original code by

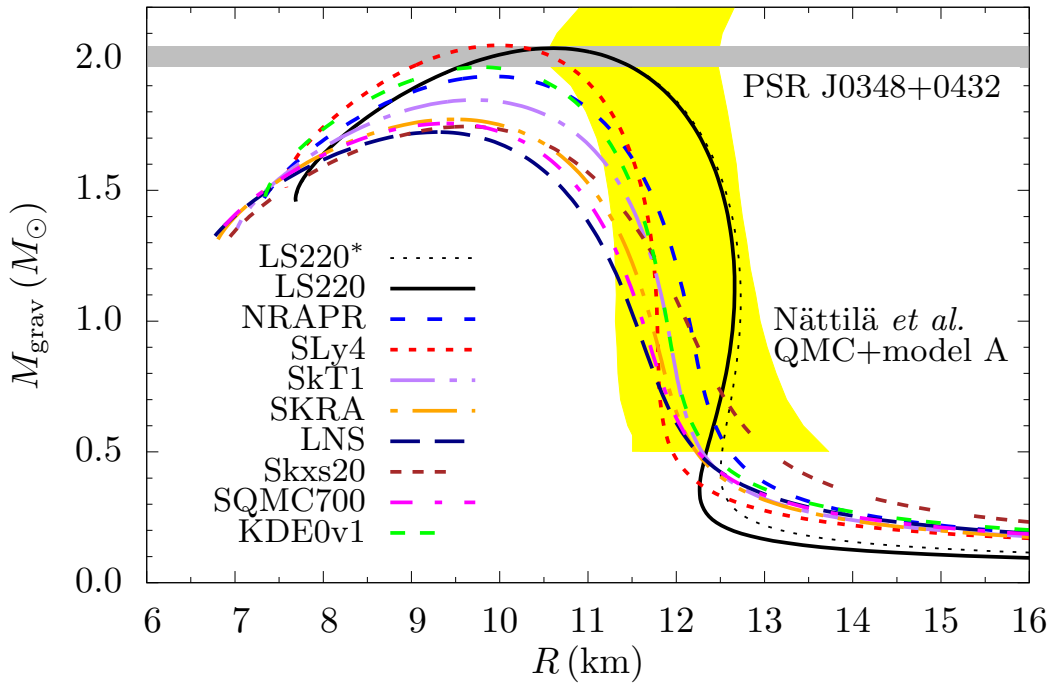

FIG. 9: (Color online) Mass-radius curves for cold, beta-equilibrated neutron stars (NSs) obtained by solving the Tolman-Oppenheimer-Volkoff equations for the considered Skyrme parametrizations. We summarize NS properties in Table IV. The gray strip represents the mass of the NS PSR J0348 + 0432, $M_{\rm J0348+0432} = 2.01 \pm 0.04 M_\odot$ [79]. The yellow region indicates the NS mass-radius constraints from model A of Nättilä *et al.* [12]. Besides the LS220 parameterization, only SLy4 and (barely) KDE0v1 and NRAPR satisfy the $M_{\rm max} \gtrsim 2\,M_\odot$ constraint. Differences between our implementation of LS220 and the original L&S implementation (LS220*) are due to the lower limit of $y \geq 0.035$ in the latter (cf. Figure 8).

L&S . The differences in the $M-R$ curves come from pressure differences in the range $10^{13}\,{\rm g\,cm^{-3}} \lesssim \rho \lesssim 10^{14}\,{\rm g\,cm^{-3}}$ that are a result of the lower proton fraction limit of $y = 0.035$ for LS220*.

Most of the considered Skyrme parametrizations are unable to support a $2\,M_\odot$ NS. To date, the most massive observed NS have masses $M_{J1614-2230} = 1.97 \pm 0.04 M_\odot$ [11] (recently revised to 1.928 ± 0.017 by Fonseca *et al.* [83]) and $M_{J0348+0432} = 2.01 \pm 0.04 M_\odot$ [79]. The latter is shown as a gray strip in Figure 9. Besides the LS220 parametrizations, only the NRAPR, SLy4, and KDE0v1 EOSs can account for the existence of $2M_\odot$ NSs.

The radius $R_{1.4}$ of a canonical $1.4\,M_\odot$ NS was constrained by Lattimer *et al.* to be in the range 10.5 to 12.5 km [84], by Guillot *et al.* to be in the 10 to 11.5 km range ([85] as updated by [14]), and by Nätillä *et al.* to be $R_{1.4} = 12.0 \pm 0.7$ km [12]. As shown in Table IV, the results for $R_{1.4}$ from all considered Skyrme parametrizations are in agreement with these constraints. Combining the results for $R_{1.4}$ with the lower limit of the maximum NS mass from observations, we see that LS220, NRAPR, SLy4, and KDE0v1 parametrizations are the ones which more closely fulfill current astrophysical constraints. Note, however, that the LS220 parametrization is an outlier and predicts $R_{1.4}$ about 1 km larger than the upper limit obtained by Guillot *et al.*

We plot density and proton fraction profiles for $1.4\,M_\odot$ NSs in Figure 10 and for maximum mass NS configurations in Figure 11. We note that the LS220 parametrization predicts lower densities and higher central proton fractions than the other parametrizations. This results from the LS220 EOS being stiffer than all other considered EOSs and having significantly different predictions for the density-dependent symmetry energy $\mathcal{S}(n)$ (cf. Equation 50 and Table II.) In the maximum-mass all NSs have central densities far above n_0 and we can again separate the EOSs into two groups. In Group I, which encompasses the LS220, SLy4,and KDE0v1 parametrizations, the proton fraction increases toward the center of the NS. In contrast, for Group II, which includes the other six parametrizations, the proton fraction decreases toward the center of the NS, even reaching $y = 0$ for SKRA, SkT1, and SQMC700.

A. High density EOS modifications

Most Skyrme parametrizations fail to produce $2M_\odot$ NSs (see, e.g., [9] and Table IV). Since $2M_\odot$ NSs have been observed in nature [11, 79, 83], a Skyrme parametrization intended for astrophysical simulations should satisfy this lower limit on the maximum NS mass. However, Skyrme parameters are often chosen to produce properties of nearly symmetric nuclear matter in the range $\sim n_0/2 - 3n_0$ while densities in the center of a NS near maximum mass may reach $\sim 10 n_0$ and matter may be very neutron rich. Under these condi-

TABLE IV: Summary of neutron star (NS) properties for the considered Skyrme parametrizations. $M_{\rm max}$ is the maximum NS mass, $R_{\rm max}$ is the radius of the maximum-mass NS, $(c_s/c)_{\rm max}$ is its central speed of sound relative to the speed of light c and $(n_c/n_0)_{\rm max}$ is its central density relative to saturation density n_0. $R_{1.4}$, $(c_s/c)_{1.4}$, and $(n_c/n_0)_{1.4}$ are the radius of a $1.4\,M_\odot$ NS, its central speed of sound, and its central density, respectively.

Parametrization	$M_{\rm max}$ $(M_\odot)$	$R_{\rm max}$ (km)	$(c_s/c)_{\rm max}$	$(n_c/n_0)_{\rm max}$	$R_{1.4}$ (km)	$(c_s/c)_{1.4}$	$(n_c/n_0)_{1.4}$
LS220 [3]	2.04	10.61	0.880	7.18	12.66	0.556	2.84
KDE0v1 [68]	1.97	9.80	0.966	7.75	11.67	0.617	3.46
LNS [69]	1.72	9.29	0.839	8.58	11.02	0.612	4.18
NRAPR [59]	1.94	9.94	0.913	7.94	11.87	0.594	3.46
SKRA [70]	1.77	9.48	0.852	8.98	11.31	0.600	4.15
SkT1 [71]	1.85	9.74	0.868	8.30	11.55	0.595	3.73
Skxs20 [72]	1.74	9.63	0.811	8.86	11.52	0.587	4.12
SLy4 [73]	2.05	9.99	0.990	7.47	11.72	0.624	3.35
SQMC700 [74]	1.76	9.40	0.853	8.60	11.16	0.609	4.06

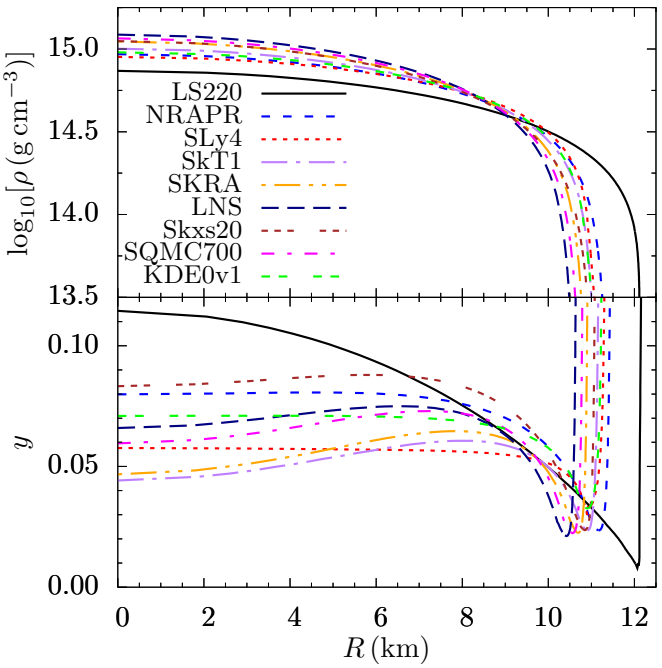

FIG. 10: (Color online) Radial rest-mass density (top panel) and proton fraction profiles (bottom panel) of cold, beta-equilibrated $1.4\,M_\odot$ neutron stars (NSs) obtained with the considered Skyrme parametrizations. Note that LS220 is an outlier, yielding the lowest central density, the largest radius, and the highest central proton fraction. This is due primarily to its large L parameter and the linear behavior of its density-dependent symmetry energy, which results in the smallest symmetry energies below saturation density and the largest symmetry energies above saturation density of all the EOS considered here (cf. Figure 1). We summarize key NS quantities in Table IV.

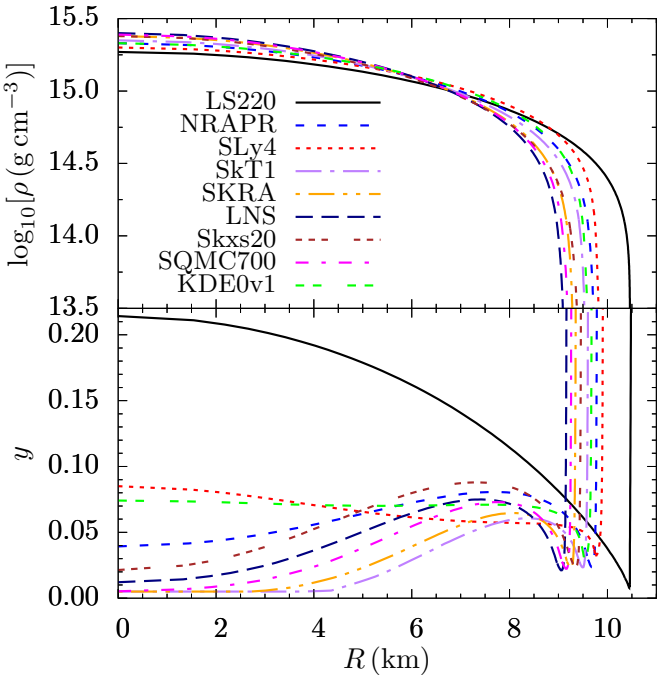

FIG. 11: (Color online) Radial rest-mass density (top panel) and proton fraction (bottom panel) profiles of cold, beta-equilibrated maximum-mass neutron stars (NSs) as predicted by the considered Skyrme parametrizations. Note that the maximum mass varies between parametrizations. Table IV summarizes key NS quantities for all parametrizations. As in the $1.4\,M_\odot$ NS case shown in Figure 10, the LS220 parametrization is an outlier and yields the lowest central density, the highest central proton fraction, and the largest radius for its maximum-mass NS configuration.

tions, the properties of matter are still fairly unconstrained. Therefore, Skyrme interactions are not expected to be valid beyond a density $n \sim 3n_0 \sim 0.5\,\mathrm{fm}^{-3}$ [9, 67]. Thus, the maximum NS mass should not be necessarily used to invalidate a Skyrme parametrization. Ideally, a model of high density matter should be matched to the Skyrme model at high densities. Dutra *et al.* use the Skyrme interaction up to about $3n_0$ and match it to a different high-density EOS at higher densities [9]. For $n \gtrsim 3n_0$, they chose a zero-temperature full quark-meson-coupling (FQMC) model [86], which includes a full baryon octet in the high-density matter and predicts $2M_\odot$ NSs, in agreement with observations. Since we are interested in finite-temperature EOSs, we instead propose a direct modification of the Skyrme parametrization that affects

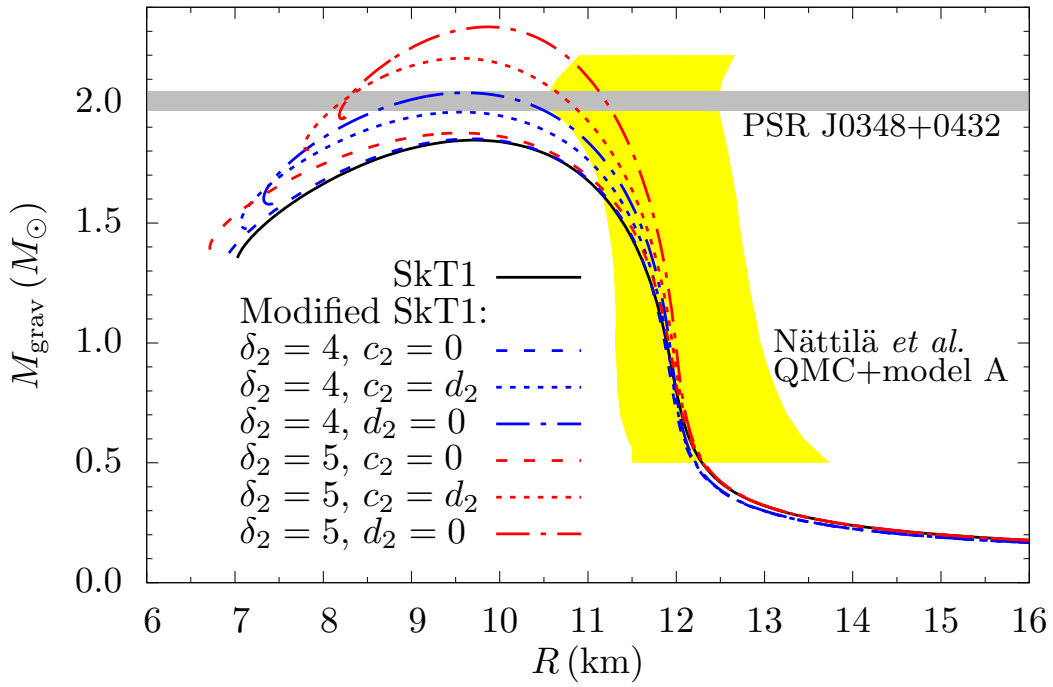

FIG. 12: (Color online) Mass-radius curves for cold, beta-equilibrated neutron stars (NS) obtained with the SkT1 parametrizations and its various high-density modifications. The gray strip represents the mass PSR J0348 + 0432 $M_{\rm J0348+0432} = 2.01 \pm 0.04 M_\odot$ [79] and the yellow region indicates the NS mass-radius constraints from model A of Nättilä *et al.* [12].

its behavior at high densities, but leaves the EOS properties at and below saturation density unchanged.

For most Skyrme parametrizations the terms $\{c_i, d_i, \delta_i\}$ in Equation (7) are only non-zero for a single value of i, *i.e.*, $i = 1$. The generalization to include extra non-zero terms is straightforward. We proceed as follows: we add an extra set of terms $\{c_2, d_2, \delta_2\}$ to the sum in Equation (7) with $\delta_2 > 3$. We adjust the values of c_2 and d_2 to minimally impact the properties of saturation-density matter. As an example of this high density EOS modification, we consider the SkT1 parametrization, which predicts a maximum NS mass of $M_{\rm max} = 1.85 M_\odot$. We add extra terms to it so that the contribution to the nuclear incompressibility $K_0 = K(n_0, 0.5)$ (see Equation 45) from the $i = 2$ term is 1% of the $i = 1$ term contribution, *i.e.*,

$$\frac{\delta_2}{\delta_1}\frac{\delta_2 - 1}{\delta_1 - 1}\frac{c_2 + d_2}{c_1 + d_1}\frac{n_0^{\delta_2}}{n_0^{\delta_1}} = 0.01. \tag{56}$$

This choice, along with $\delta_1 < \delta_2 \lesssim 10$, leaves all nuclear matter properties at saturation density n_0 well within current known experimental constraints, but significantly increases the pressure at high densities.

We study here six modified SkT1 parametrizations. Besides the choice defined by Equation (56), we chose the exponent values $\delta_2 = 4$ and 5, and set the constants c_2 and d_2 such that $c_2 = 0$, or $d_2 = 0$, or $c_2 = d_2$.

In Figure 12, we plot NS mass-radius curves for these modified parametrizations. We summarize key properties of the TOV NS sequences in Table V. Both figure and table show, as expected, that the higher the exponent δ_2 and the larger c_2 is with respect to d_2, the stiffer the EOS for cold BEM becomes. This results in a higher maximum NS mass and a larger radius for the $1.4 M_\odot$ NS. The main drawback of the proposed modifications is that the speed of sound increases significantly for densities above $3 n_0$. It becomes superluminal at densities lower than those at the center of maximum-mass NSs (cf. Table V). Nevertheless, the modifications can be useful for studying the impact of a higher maximum NS mass on astrophysical simulations while keeping the properties of saturation-density nuclear matter fixed.

VI. ADIABATIC COMPRESSION

To check the thermodynamic consistency of our code and of the EOS tables it generates, we perform adiabatic compression tests. An isolated system that is slowly compressed from a lower to a higher density should retain its initial entropy. To test this, we generate EOS tables for different Skyrme parametrizations in the ranges of density n, temperature T, and proton fraction y, given in Table VI. We set the table resolution to 30 points per decade in temperature and density and 1 point every 0.01 in proton fraction. We also consider tables with double the resolution across each EOS dimension. The lower resolution is similar to that of the tables available at https://stellarcollapse.org/equationofstate. These older tables are described by O'Connor & Ott in [50] and have been used frequently in astrophysical simulations. Following [50], we interpolate trilinearly in n, T, and y. We find T for a given n, y, and specific

TABLE V: Summary of neutron star (NS) properties for the SkT1 parametrization and its high-density modifications. $M_{\rm max}$ is the maximum NS mass, $R_{\rm max}$ is the radius of the maximum-mass NS, $(c_s/c)_{\rm max}$ is its central speed of sound relative to the speed of light c and $(n_c/n_0)_{\rm max}$ is its central density relative to saturation density n_0. $R_{1.4}$, $(c_s/c)_{1.4}$, and $(n_c/n_0)_{1.4}$ are the radius of a $1.4\,M_\odot$ NS, its central speed of sound, and its central density, respectively. Note that the central speed of sound in the maximum-mass NS is superluminal for most of the modified EOSs.

Parametrization	$M_{\rm max}$ $(M_\odot)$	$R_{\rm max}$ (km)	$(c_s/c)_{\rm max}$	$(n_c/n_0)_{\rm max}$	$R_{1.4}$ (km)	$(c_s/c)_{1.4}$	$(n_c/n_0)_{1.4}$
SkT1 [71]	1.85	9.74	0.868	8.30	11.55	0.595	3.73
$\delta_2 = 4,\ c_2 = 0$	1.85	9.65	0.891	8.49	11.55	0.597	3.69
$\delta_2 = 4,\ c_2 = d_2$	1.96	9.59	1.091	8.11	11.63	0.608	3.55
$\delta_2 = 4,\ d_2 = 0$	2.04	9.58	1.209	7.92	11.68	0.616	3.45
$\delta_2 = 5,\ c_2 = 0$	1.88	9.56	0.989	7.85	11.60	0.602	3.37
$\delta_2 = 5,\ c_2 = d_2$	2.19	9.56	1.533	6.84	11.73	0.638	3.12
$\delta_2 = 5,\ d_2 = 0$	2.32	9.88	1.615	6.23	11.83	0.655	2.98

TABLE VI: Ranges in density n, temperature T, and proton fraction y, and the number of EOS table points in each dimension for our standard-resolution EOS tables. The high-resolution tables have the same range, but contain twice the number of points in each dimension.

Parameter	minimum	maximum	points
$\log_{10}[n(\mathrm{fm}^{-3})]$	-12.2	0.8	391
$\log_{10}[T(\mathrm{MeV})]$	-3.0	2.4	163
y	0.005	0.655	66

internal energy ϵ or specific entropy s via Newton-Raphson root finding.

In our adiabatic compression tests, for a given proton fraction, we set the system to an initial temperature $T = 10^{-2}\,\mathrm{MeV}$ and determine the initial densities for which the entropy has values of 0.1, 0.2, 0.5, and $1.0\,k_B\,\mathrm{baryon}^{-1}$. Every step, the density is increased by $\delta n = 10^{-3} n$ until the system reaches a density of $1\,\mathrm{fm}^{-3}$ or its temperature excedes the maximum of our tables ($T_{\rm max} = 250\,\mathrm{MeV}$). As the system is compressed, we integrate the first law of thermodynamics using a fourth-order Runge-Kutta integrator and determine the ratio of the entropy $s(n)$ to the initial entropy s_0 as a function of density. As a representative example result, we show in Figure 13 the fractional changes in entropy during the compression for both the high-resolution and standard-resolution SLy4 tables.

We see from Figure 13 that for specific entropies of $s \gtrsim 0.5\,k_B\,\mathrm{baryon}^{-1}$ and proton fractions $y \gtrsim 0.3$, even the standard-resolution tables yield nearly perfectly adiabatic compression. This bodes very well for stellar collapse and CCSN simulations, since entropies always stay higher than $0.5\,k_B\,\mathrm{baryon}^{-1}$ and proton fractions below ~ 0.3 are not reached until the final phase of collapse.

At lower entropies and proton fractions, we observe substantial deviations from adiabatic compression with entropy errors of order 10% or greater with the standard-resolution tables. This issue is largely numerical and due to interpolation and root-finding errors, since the high-resolution tables yield much better results. However, large changes in entropy can still occur near the first-order phase transition between non-uniform and uniform nuclear matter near $n \simeq 10^{-1}\,\mathrm{fm}^{-3}$.

For comparison, we carry out adiabatic compression tests also for the tables of [50]. We find that even our standard-resolution tables yield smaller entropy errors than any of the EOS tables of [50] available at https://stellarcollapse.org/equationofstate.

Finally, adding a transition from SNA to NSE at low densities, as we discuss below in Section VII A, only leads to small quantitative changes compared to the results presented in this section.

VII. APPLICATION TO STELLAR CORE COLLAPSE

We carry out a set of example core collapse and postbounce CCSN simulations to investigate how our new EOSs perform in this important astrophysical scenario and how they influence core collapse, postbounce evolution, and black hole formation. Before discussing the CCSN simulations, we describe how we modify our EOSs at low density to include an ensemble of nuclei in NSE.

A. Nuclear statistical equilibrium (NSE)

NSE holds for temperatures $T \gtrsim 0.5\,\mathrm{MeV}$ at which forward and backward nuclear reaction rates are so high that equilibrium is obtained faster than any other timescale in the system. At low density and moderate temperatures, the NSE equilibrium state of matter includes an ensemble of nuclear species (nuclides) and SNA is not a good approximation for describing the thermodynamics. SNA predicts different thermodynamic quantities, average nuclear binding energies, and neutrino opacities than a model assuming NSE [87, 88]. Furthermore, SNA predicts a single average nucleus whose properties can differ significantly from the observed properties of nuclei due to shell closures, pairing, and many body-body effects missing from the simple liquid-drop SNA. Conversely, NSE breaks down at high densities when interactions between the nuclear interior and the surrounding medium become important. This can be partially overcome by including excluded volume corrections in the NSE formulation [40].

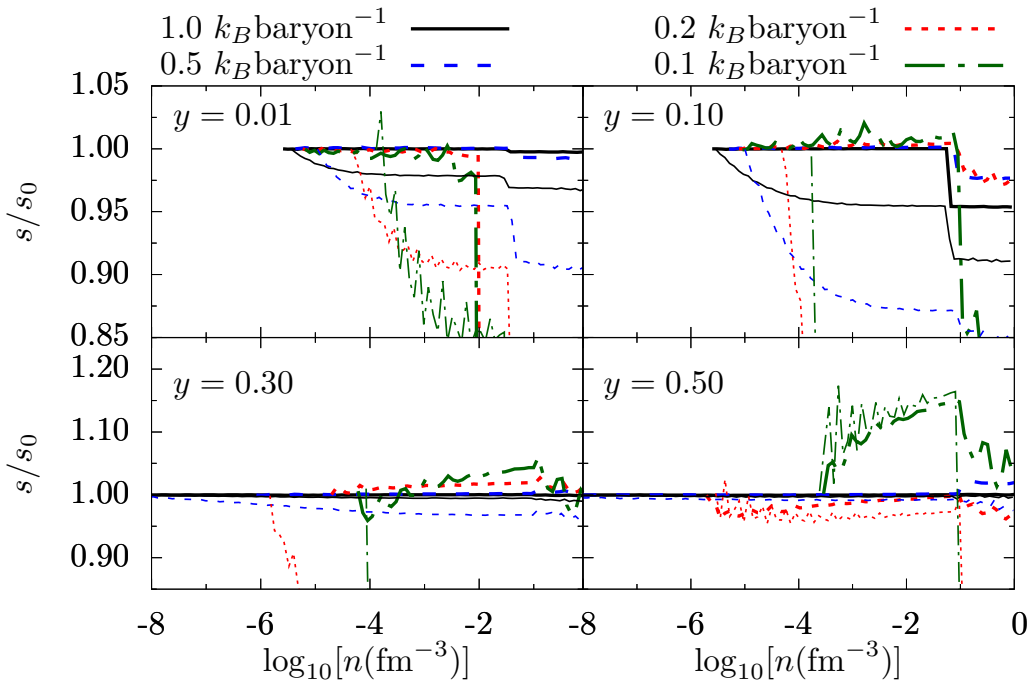

FIG. 13: (Color online) Relative error in the specific entropy as a function of density during adiabatic compression tests with the full EOS based on the SLy4 parametrization and the single-nucleus approximation at all densities. The different panels show results for proton fractions $y = 0.01, 0.10, 0.3$, and 0.5. All curves start at $T = 0.01$ MeV and we choose the initial densities to obtain starting values of the specific entropy of $s_0 = 0.1$, 0.2, 0.5, and $1.0\,k_B$ baryon^{-1}. Thick (thin) curves correspond to tests with the high (standard) resolution tables (cf. Table VI). For $s_0 \gtrsim 0.5\,\mathrm{k_B}$ baryon^{-1} and proton fractions $y \gtrsim 0.3$, the standard-resolution tables perform very well. In stellar collapse, the specific entropy always stays higher than $0.5\,\mathrm{k_B}$ baryon^{-1} and proton fractions below $\sim$0.3 are not reached until the final phase of collapse. Errors at lower s_0 and y are largely numerical and are reduced by employing the high resolution table. However, large changes in entropy can still occur near the first-order phase transition between non-uniform and uniform matter at $n \simeq 0.1\,\mathrm{fm}^{-3}$.

However, such an approach does not account for changes in nuclear shapes and requires a very large, neutron rich ensemble of nuclei to reasonably reproduce the high density, low proton fraction composition. To alleviate the aforementioned issues with the SNA while still retaining its advantages at high density, we transition from SNA to an NSE EOS at densities where nuclear interactions are small and SNA and NSE can be smoothly matched.

Another reason for transitioning from the SNA to NSE is that at low density and temperature, the abundances of nuclei can fall out of equilibrium, which requires smoothly transitioning from material in NSE to following a network of reactions between separate nuclides. To perform such a transition in a thermodynamically consistent manner, the same set of nuclei and nuclear partition functions must be used to calculate both the equilibrium number densities and for the non-equilibrium evolution. The SNA will not satisfy this consistency condition, but it can be easily enforced by using an NSE EOS at moderate temperature and density.

For completeness, we provide a full discussion of our standard treatment for an ensemble of nuclei in NSE in Appendix B. Once the free energy densities for the SNA and NSE phases, $F_{\rm SNA}$ and $F_{\rm NSE}$, respectively, have been determined, we combine the two using a density dependent function $\chi(n)$, *i.e.*,

$$F_{\rm MIX} = \chi(n) F_{\rm SNA} + [1 - \chi(n)] F_{\rm NSE}\,. \tag{57}$$

Here, the SNA (NSE) subscripts denote the contribution to the thermodynamical quantities from the high (low) density parts of the EOS. $F_{\rm SNA}$ is given by Equation (2) while $F_{\rm NSE}$ is given by Equation (B6). The limits of the function $\chi(n)$ are chosen so that it goes to zero at low densities and to one at high densities. We mix the two using the smooth choice for $\chi(n)$,

$$\chi(n) = \frac{1}{2}\left[1 + \tanh\left(\frac{\log_{10}(n) - \log_{10}(n_t)}{n_\delta}\right)\right], \tag{58}$$

where n is the density of the system, n_t the center of the transition, and n_δ its width. We set the center of the transition density $n_t = 10^{-4}\,\mathrm{fm}^{-3}$ ($\simeq 1.7 \times 10^{11}\,\mathrm{g\,cm}^{-3}$) and its dimensionless width $n_\delta = 0.33$. This choice guarantees that the transition happens in a region where differences in the nuclear contributions to the total pressure, entropy, and energy density in the NSE and SNA treatments are relatively small, at least for matter with small isospin asymmetry, where EOS constraints are more accurately known. Furthermore, this transition is at sufficiently low densities that the

EOS is dominated by the electron (photon) contribution at low (high) temperatures. At the same time, the transition density is high enough that above n_t we expect large deformed nuclei and the pasta phases to dominate, which are well described in the SNA approximation.

Because $\chi(n)$ is density dependent, the transition procedure introduces corrections to the pressure and other derivatives with respect to density in the transition region that are of order $F_{\rm SNA} - F_{\rm NSE}$. For example, in the mixing region, the pressure is given by

$$\begin{aligned} P_{\rm MIX} &= n^2 \left.\frac{\partial (F_B/n)}{\partial n}\right|_{T,y} \\ &= \chi(n) P_{\rm SNA} + [1-\chi(n)] P_{\rm NSE} \\ &\quad + n^2 \frac{\partial \chi(n)}{\partial n} \left(F_{\rm SNA} - F_{\rm NSE}\right) . \end{aligned} \tag{59}$$

Other quantities are readily computed. In practice, we find that the corrections due to $\chi(n)$ are small compared to the other contributions to the free energy. Although this procedure is ad-hoc, it results in a thermodynamically consistent EOS and does not require the calculation of a more complicated phase transition.

B. Stellar Collapse

To study the impact of our new EOSs on stellar collapse, we employ the open-source spherically-symmetric (1D) general-relativistic hydrodynamics code `GR1D` [50–52]. For simplicity and efficiency, we employ its neutrino leakage/heating scheme described in [50] and postpone detailed radiation-hydrodynamics studies using `GR1D`'s two-moment transport solver to future work. Deleptonization during the collapse phase is handled via a parametrization of the proton fraction y as a function of rest-mass density ρ as proposed by Liebendörfer [89] with the parameters given in [50]. `GR1D`'s EOS routines interpolate tabulated thermodynamic variables such as pressure, specific internal energy, specific entropy, etc. linearly in $\log_{10}\rho$, $\log_{10} T$, and y, and do not obtain them via the interpolated free energy (and its derivatives). This means that thermodynamic consistency is not guaranteed, is subject to interpolation errors and EOS table resolution, and must be checked [90].

We study core collapse and postbounce evolution in two progenitor stars: (1) In the 15-$M_\odot$ progenitor of Woosley and Weaver (W&W hereafter) [91], which has been used widely in the literature. (2) In the 40-$M_\odot$ progenitor of Woosley and Heger (W&H hereafter) [92], which has a very massive, high-compactness core and is expected to form a black hole (BH) [51]. For the 15-$M_\odot$ progenitor, we use a computational grid with 1000 grid cells, constant cell size of $100\,\mathrm{m}$ out to a radius of $20\,\mathrm{km}$, and then geometrically increasing cell size to an outer radius of $10\,000\,\mathrm{km}$. For the 40-$M_\odot$ progenitor, whose collapse we evolve until BH formation, we use 1500 grid cells, a constant cell size of $75\,\mathrm{m}$ out to $25\,\mathrm{km}$, and geometrically increasing cell size to an outer radius of $10\,000\,\mathrm{km}$.

Stellar evolution codes use EOSs (e.g., [93]) that can differ substantially from the EOSs presented in this paper. On the one hand, in the NSE region, the predicted pressure, entropy, etc. depend on the number of nuclides tracked in the stellar model. On the other hand, in the non-NSE region, compositional details will depend on the employed nuclear reaction network and, again, composition will affect the thermodynamical variables. These differences between EOSs are not negligible for core collapse simulations: at the onset of collapse, small variations in the pressure profile between stellar and core collapse EOSs can alter the hydrodynamics of the core, and may accelerate or delay collapse.

In order to start our simulations in a way that is as consistent as possible with the hydrodynamical structure of our progenitor models, we map the stellar rest-mass density ρ, proton fraction y, and pressure P to `GR1D`, and then find temperature T (and specific internal energy, entropy, etc.) using the EOS table. We stress that our approach for setting up the initial conditions results in differences between the original stellar profile and the `GR1D` initial conditions in all quantities except ρ, y, and P. Also note that for the purpose of this study, we assume NSE throughout the part of the star mapped to `GR1D`'s grid. This is an approximation that will need to be relaxed in the future, since the outer regions of the core and the silicon-rich and oxygen-rich layers are not in NSE.

In most of our core collapse simulations, we use our standard-resolution EOS tables described in Table VI. Our adiabatic compression tests in Section VI suggest that higher resolution tables lead to more accurate adiabatic collapse results, in particular for low entropies. However, in our collapse simulations, entropies are always sufficiently high that using our standard-resolution tables yields excellent results. Tests with the high-resolution tables show only negligible differences in the simulation results. Only in the case of very stiff EOS, such as SkT1* (see below), we find it necessary to use higher-resolution tables to accurately track simulations on the route to BH formation at central proto-NS densities above $\sim 10^{15}\,\mathrm{g\,cm^{-3}}$.

1. 15-$M_\odot$ *Progenitor*

We follow core collapse and postbounce evolution up to $1.2\,\mathrm{s}$ after bounce in the 15-$M_\odot$ progenitor. While this star is expected to explode in nature (e.g., [94]), we use the default scaling factor $f_{\rm heat} = 1$ for neutrino heating in `GR1D` and do not obtain an explosion in our `GR1D` simulations. This is consistent with more elaborate 1D radiation-hydrodynamic simulations (e.g., [95]).

In a first set of simulations, we focus on the effects of different Skyrme parametrizations. We employ ten different EOSs – the nine Skyrme parametrizations discussed in Section IV and one of the modified versions of the SkT1 parametrizations stiffened at high density studied in Section V A. We call this parametrization SkT1* and use $\delta_2 = 5$, $d_2 = 0$, which produces the highest cold NS mass for SkT1. We merge the SNA Skyrme EOSs with an NSE EOS containing 3 335 nuclides following the prescription detailed in Section VII A.

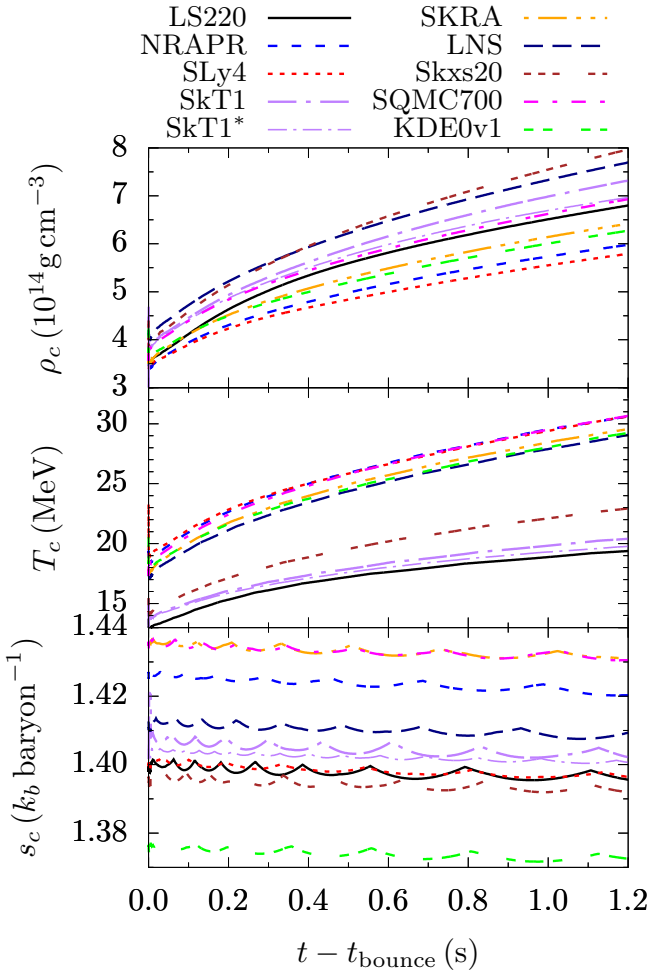

FIG. 14: (Color online) Results from core collapse simulations with the 15-$M_\odot$ progenitor and EOSs generated with various Skyrme parametrizations and a 3 335-nuclide NSE EOS at low densities. From top to bottom, we show 1.2 s of postbounce evolution of the central density ρ_c, central temperature T_c, and central specific entrop s_c. Note that the entropy stays roughly constant (modulo mild numerical oscillations) throughout the postbounce evolution, as it should for thermodynamically consistent EOSs. As postbounce accretion adds mass to the proto-NS, it contracts, which is marked by an increase in ρ_c and softer EOSs result in a steeper increase. The splitting of the T_c evolutions into two groups of parametrizations can be understood by considering that those resulting in lower temperatures have a larger effective nucleon mass (see Section II A and Table II).

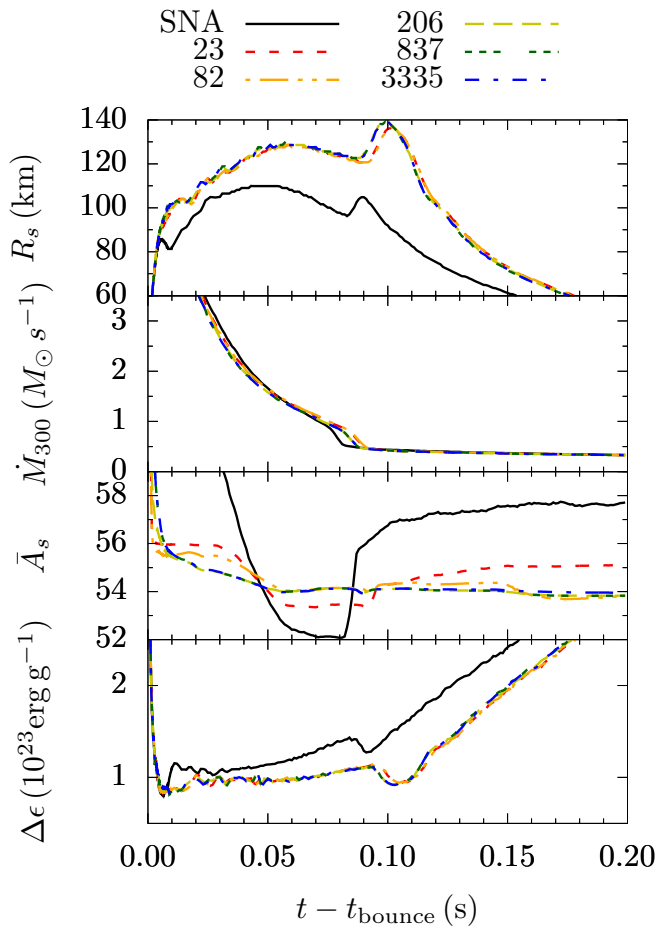

FIG. 15: (Color online) Results of core collapse simulations with the 15-$M_\odot$ progenitor and the LS220 Skyrme parametrization. We compare results obtained for pure SNA (at all densities) with results from simulations that use SNA at high densities, smoothly matched to an NSE EOS with varying number of nuclides at low densities (see Section VII A for details). From top to bottom, we plot the postbounce evolution of shock radius R_s, accretion rate $\dot{M}_{300}$ at a radius of 300 km, average nuclear mass number 5 km above the shock, and difference in specific internal energy, $\Delta\epsilon$ 5 km above and 5 km below the shock. Note that the pure-SNA simulation predicts a substantially smaller shock radius than the SNA+NSE simulations. This is a consequence of the SNA shock having to break up more bound nuclei, reflected in greater $\Delta\epsilon$ across the shock.

We employ a transition density $n_t = 10^{-4}\,\mathrm{fm}^{-3}$ ($\rho_t \simeq 1.67 \times 10^{11}\,\mathrm{g\,cm}^{-3}$) and dimensionless width of $n_\delta = 0.33$ (cf. Equation 58).

The time from the onset of collapse to core bounce is approximately the same for all simulations, $t_{\mathrm{bounce}} = 0.331 \pm 0.008$ s, since it is mostly a function of the low density part of the EOS, which is the same for all tables which include NSE at low densities. In Figure 14, we plot the postbounce evolution of the central density, central temperature, and central specific entropy resulting from the 10 different Skyrme parametrizations. As the proto-NS's mass increases due to the settling of material that accretes through the stalled supernova shock, its core is adiabatically compressed since the time scale for neutrino diffusion is much longer than the accretion time scale. Core density and temperature increase, while the central entropy stays nearly constant over the 1.2 s of postbounce time we simulate. The latter is a further demonstration of the thermodynamic consistency of our EOSs. We attribute the small wiggles and the small secular drift in the central entropy to interpolation errors and the finite resolution of our EOS tables.

The postbounce central density and temperature evolutions shown in Figure 14 exhibit significant dependence on

Skyrme parametrization. The ordering of the central density evolution and its slope roughly follows the stiffness of the EOS. Softer EOSs (lower maximum NS mass) have higher densities at bounce and a steeper postbounce slope in ρ_c than stiffer EOSs. The two bracketing cases are SLy4 ($M_{\rm max} \sim 2.05 M_\odot$) and Skxs20 ($M_{\rm max} \sim 1.74\,M_\odot$). Note that the SkT1 and the SkT1* parametrizations start out at the same ρ_c at bounce, but that the slope of ρ_c in the SkT1* simulation becomes gradually shallower as the proto-NS contracts. This is a direct consequency of the stiffened high-density part of SkT1*.

The T_c evolution in Figure 14 is divided into two groups. In the first group, containing LS220, Skxs20, SkT1, and SkT1*, T_c right after bounce is $\sim 13-15\,{\rm MeV}$ and rises to $T_c \sim 19-22\,{\rm MeV}$ within the first second after bounce. For the second group, containing all other parametrizations, we find $T_c \sim 17-19\,{\rm MeV}$ right after bounce, rising to $\sim 28-30\,{\rm MeV}$ a second after bounce. These pronounced differences in core temperatures result from different treatments of the nucleon effective masses in Equations (7) and (8) with the parameters in Table II. At a fixed density and proton fraction, the thermal contribution to the free energy of uniform matter only depends on the chosen Skyrme parametrization through the effective masses, at least in the mean field approximation. For non-relativistic particles, temperature enters the baryon entropy for fixed neutron and proton densities only through the combinations $m_t^* T$. Therefore, if $m_t^* \approx m_t$, then temperatures at similar density and entropy will be smaller than in cases where $m_t^* < m_t$. This explains the T_c-grouping in Figure 14.

In a second set of simulations with the 15-$M_\odot$ progenitor, we investigate the sensitivity of the collapse and postbounce evolution to the number of nuclides included in the low-density NSE part of the EOS. We choose the frequently used LS220 Skyrme parametrization for the high-density SNA part and match it to a set of low-density NSE EOSs with 23, 82, 206, 837, and 3 335 nuclides, using the same matching parameters as before. Each larger list of nuclides includes all of the nuclides of the smaller nuclide lists and we provide all lists at https://stellarcollapse.org/SROEOS. We also carry out a simulation with an EOS table that uses the SNA at all densities.

Since the low-density EOS is dominated by relativistic degenerate electrons, differences in the number of NSE nuclei have only a mild effect on the collapse dynamics. We find times to core bounce that vary by less than 2 ms. The SNA simulation reaches bounce at 0.334 s, while all simulations that include nuclides in NSE reach bounce within a very similar time, $t_{\rm bounce} = 0.332 \pm 0.001$ s. The close agreement of the SNA and NSE bounce times is particular to the LS220 parametrization and the 15-$M_\odot$ progenitor. For the same progenitor and other parameterizations, we find that SNA simulations reach bounce up to $20-30$ ms later than NSE simulations. For other progenitor stars that have lower-density cores at the onset of collapse, the differences can be even larger (see Section VII B 2, where we discuss results for a 40-$M_\odot$ progenitor).

In Figure 15, we plot the postbounce evolution of the shock radius, the mass accretion rate at a radius of 300 km, average nuclear mass number $\bar{A}$ at 5 km above the shock, and the difference $\Delta\epsilon$ in specific internal energy between 5 km above and 5 km below the shock. We focus on the first 200 ms of postbounce evolution.

The most striking and important difference between simulations using SNA and NSE in the low-density regime are apparent in the shock radius evolution. Consistently, and independent of number of nuclides in NSE, simulations with an NSE treatment yield substantially larger shock radii than the SNA simulation. In the case of the LS220 parametrization shown here, around 50 ms (100 ms) after bounce, the shock radius difference between the two treatments is $\sim$25 km ($\sim$50 km). The cause of this difference can be inferred from the two bottom panels of Figure 15: In the NSE case, the preshock nuclei are generally less bound and $\Delta\epsilon$ is smaller than in the SNA case. Hence, the shock in the NSE simulations has to do less work to dissociate nuclei and can thus achieve larger radii. We find similar systematics between NSE and SNA simulations for all our Skyrme parametrizations. The radius at which the shock stalls can have an important impact on the subsequent CCSN evolution (e.g., [96]) and, generally, the larger the radius at which the shock stalls, the better the chances for a successful explosion. Our above findings thus emphasize the need for a many-nuclide (NSE) treatment of the low-density EOS in CCSN simulations.

The second panel of Figure 15 shows that the evolution of the postbounce accretion rate is only mildly sensitive to SNA/NSE and the number of nuclides employed in the NSE EOS. Though one notes that the SNA leads to higher early accretion rates and a slightly earlier drop in the accretion rate, since the density discontinuity that is present at the edge of the iron core in the 15-$M_\odot$ progenitor reaches small radii and the shock earlier. This is also reflected in the shock radius evolution, which shows a pronounced excursion when the density drop reaches the shock.

From the third panel of Figure 15, showing the average nuclear mass $\bar{A}$ just above the shock, we note that $\bar{A}$ and the nuclear binding energy predicted by the LS220 SNA is very different from what NSE predicts. It also appears that one needs in excess of $\sim$82 nuclides for NSE to predict a converged $\bar{A}$, though this is likely sensitive to the specific set of nuclides included. The large differences in $\bar{A}$ and nuclear binding energy translate to the differences in $\Delta\epsilon$ shown in the bottom panel. These, in turn, explain the different shock radii plotted in the top panel and discussed in the above.

2. 40-$M_\odot$ *Progenitor*

The 40-$M_\odot$ progenitor is expected to result in BH formation with no or only a very weak explosion (e.g., [51]). We carry out two sets of simulations with this progenitor. In the first set, we employ ten different Skyrme parametrizations combined with a 3 335-nuclide NSE EOS at low densities using the same matching parameters as in the previous Section VII B 1. In the second set, we use the same Skyrme parametrization, but with SNA at all densities. We summa-

TABLE VII: Bounce time $t_{\rm bounce}$, BH formation time $t_{\rm BH}$, $t_{\rm BH} - t_{\rm bounce}$, and proto-neutron star maximum gravitational mass M_g for the $40 M_\odot$ progenitor of W&H. Results are for EOSs using different Skyrme parametrizations in the single-nucleus approximation (SNA) and in the SNA merged with an NSE EOS at $n_t = 10^{-4}\,{\rm fm}^{-3}$ with $n_\delta = 0.33$, see Section VII A. SkT1* is the modified versions of the SkT1 parametrization studied in Section V A with $\delta_2 = 5$ and $d_2 = 0$.

EOS	SNA+NSE				SNA			
	$t_{\rm bounce}$ (s)	$t_{\rm BH} - t_{\rm bounce}$ (s)	$t_{\rm BH}$ (s)	M_g ($M_\odot$)	$t_{\rm bounce}$ (s)	$t_{\rm BH} - t_{\rm bounce}$ (s)	$t_{\rm BH}$ (s)	M_g ($M_\odot$)
LS220 [3]	0.490	0.591	1.081	2.260	0.513	0.565	1.078	2.275
KDE0v1 [68]	0.490	0.938	1.428	2.435	0.515	0.914	1.429	2.441
LNS [69]	0.490	0.547	1.037	2.244	0.525	0.515	1.040	2.255
NRAPR [59]	0.491	0.916	1.407	2.427	0.531	0.873	1.404	2.442
SKRA [70]	0.491	0.757	1.248	2.352	0.532	0.716	1.248	2.371
SkT1 [71]	0.489	0.506	0.994	2.212	0.530	0.478	1.008	2.214
SkT1*[71]	0.489	0.780	1.269	2.333	0.532	0.741	1.273	2.334
Skxs20 [72]	0.488	0.438	0.926	2.178	0.545	0.406	0.951	2.182
SLy4 [73]	0.493	1.063	1.556	2.495	0.630	0.936	1.566	2.525
SQMC700 [74]	0.493	0.681	1.174	2.316	0.741	0.488	1.229	2.368

rize key simulation results in Table VII for both sets to facilitate comparison.

In Figure 16, we present the postbounce central density ρ_c, central temperature T_c, and central entropy s_c evolutions in the model set with an NSE treatment at low densities. First, we note that the central entropy stays roughly constant as it should (modulo numerical noise) throughout the evolution to BH formation. Proto-NS collapse and BH formation is marked by a dramatic increase in the slope of ρ_c, which is mirrored by T_c. At this point, the `GR1D` simulations crash, since the formulation of Einstein's equations used in `GR1D` does not permit the evolution to continue beyond BH formation (see [50] for details).

The time to BH formation is sensitive to the Skyrme parametrization and set by accretion rate and the maximum proto-NS mass that can be supported by the parametrization. Comparing the maximum mass entries in Table IV with those in Table VII, we note that the maximum proto-NS mass is systematically $0.2 - 0.6\,M_\odot$ higher than the maximum cold NS mass. As shown by O'Connor & Ott [51], this is a consequence of thermal pressure support in the proto-NS mantle where shocked material is compressed, reaching temperatures in excess of $100\,{\rm MeV}$ at late times. As discussed in the context of the 15-$M_\odot$ progenitor in Section VII B 1, Skyrme parametrizations that yield small effective nucleon masses result in higher temperatures. In turn, such parametrizations produce proto-NSs with more thermal pressure support and see a greater increase in the maximum mass from cold NS to hot proto-NS. For example, LS220, which has $m_t^\star = m_t$ and a maximum cold NS mass of $2.04\,M_\odot$, has a proto-NS mass of $2.26\,M_\odot$ at BH formation ($\Delta M = 0.22\,M_\odot$). The SLy4 parametrization has a cold NS mass of $2.05\,M_\odot$, but its proto-NS collapses at a mass of $2.491\,M_\odot$ ($\Delta M = 0.441\,M_\odot$). This is a direct consequence of SLy4's low effective nucleon masses ($m_t^\star = 0.695\,m_t$; cf. Table II) and the consequently much higher temperatures reached in its proto-NS.

Like LS220, the SkT1 parametrization also has large effective nucleon masses, resulting in lower temperatures. Its maximum cold NS mass is $1.85\,M_\odot$ and the proto-NS collapses at $2.212\,M_\odot$ ($\Delta M = 0.362\,M_\odot$). Its variant SkT1* that we stiffened at high density (see Section V A and Table V) has a maximum cold NS mass of $2.32\,M_\odot$. Interestingly, its proto-NS collapses at a mass of only $2.333\,M_\odot$ ($\Delta M = 0.013\,M_\odot$). This at first surprising result can be understood by considering that the SkT1* stiffening affects only the cold high density core, but not the hot proto-NS mantle, where most of the extra mass is located. The softness of the SkT1 parametrization combined with the relatively modest temperatures reached in the mantle thus explain our result for SkT1*'s proto-NS mass at BH formation.

In Table VII, we compare the times to core bounce and BH formation between simulations run with SNA at high densities and an NSE EOS at low densities (SNA+NSE) and with SNA at all densities. First we note that in the SNA+NSE case the time to core bounce is insensitive to the Skyrme parametrization since the transition to dynamical collapse is controlled by the NSE part that is identical in all simulations. In the pure SNA simulations, this is different and the time to core bounce can vary by hundreds of milliseconds between some parametrizations. This is a consequence of the metastability of the inner iron core at the onset of collapse where small EOS differences can have substantial impact on when the collapse becomes fully dynamical.

Finally, comparing BH formation times $t_{\rm BH}$ (measured from the start of the simulation) predicted by SNA+NSE and pure SNA simulations for a given Skyrme parametrization, we note that $t_{\rm BH}$ appears insensitive to the low-density EOS treatment. This can be understood by recalling that much of the material that is accreted by the proto-NS to reach its maximum mass comes from regions in the outer core and silicon and oxygen shells. These regions are initially in hydrostatic equilibrium since our simulations preserve the pressure stratification from the precollapse stellar profile. Once the rarefaction wave from the core's collapse reaches these regions, they proceed to collapse with supersonic velocities in free fall. Hence, the collapse of the outer regions is much less sensitive to variations in the EOS than the collapse of the initially metastable inner core.

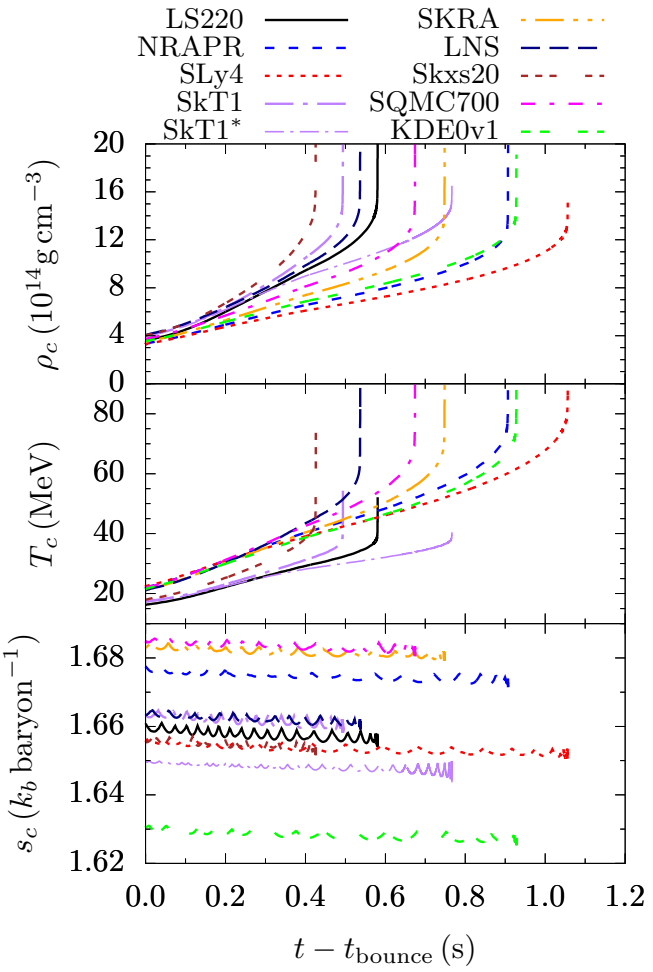

FIG. 16: (Color online) From top to bottom we plot the postbounce time evolution of the central density ρ_c, central temperature T_c, and central specific entropy s_c for the black hole (BH) formation simulations with the $40M_\odot$ progenitor. Proto-NS collapse and BH formation are marked by a sudden extreme steepening of the ρ_c slope. The different graphs correspond to simulations with different Skyrme parametrizations. We employ a 3 335-nuclide NSE EOS at low densities (cf. Section VII A). Note that the specific entropy stays, as it should, roughly constant (modulo numerical noise that can be reduced with higher-resolution EOS tables) throughout the postbounce evolution and up to BH formation. Thermal pressure support in the proto-NS mantle plays an important role in supported proto-NS masses that are $0.2-0.6\,M_\odot$ higher than the maximum cold NS mass. Thermal contributions are largest for those parametrizations that result in low effective nucleon masses and higher proto-NS temperatures.

VIII. CONCLUSIONS

In the twenty-six years since the seminal Lattimer & Swesty (L&S) paper [3] describing their finite-temperature nuclear equation of state (EOS), much progress has been made in both astrophysics simulation capability and in experimental and astrophysical constraints on the nuclear EOS. The L&S EOS has had tremendous impact on simulations of core-collapse supernovae (CCSNe) and neutron star (NS) mergers. This is due not least to L&S providing their EOS code as open source to the community.

In this study, we built upon the work of L&S and presented a generalized method for generating EOSs for CCSN and NS matter, using the compressible non-relativistic liquid-drop model with the Skyrme interaction. With this paper, we make publicly available a modern, modular, and parallel Fortran 90 code for building EOS tables for application in CCSN and NS merger simulations. The code and EOS tables for the Skyrme parametrizations considered in this paper are available at http://stellarcollapse.org/SROEOS.

Our method differs from the original L&S approach in the following significant ways: (1) EOSs can be generated for most[5] Skyrme parametrization in the literature and for future parametrizations. This feature will facilitate EOS parameter studies in astrophysics simulations within a consistent EOS framework. (2) Our method includes nucleon effective masses different from the rest masses and we obtain nuclear surface properties self-consistently for each parametrization. (3) Instead of relying on Maxwell constructions that must be pre-computed for each parametrization, we treat the transition from non-uniform to uniform nuclear matter as a first-order phase transition that is determined as the EOS is calculated. (4) The EOS obtained in the single-nucleus approximation (SNA) can be smoothly merged at low densities with a nuclear-statistical-equilibrium (NSE) EOS containing thousands of nuclides. (5) We provide for the possibility of introducing additional terms to Skyrme parametrizations that stiffen the EOS above saturation density. (6) Our method converges reliably over a wide range of temperatures ($10^{-4}\,\mathrm{MeV} \lesssim T \lesssim 10^{2.5}\,\mathrm{MeV}$), proton fractions ($10^{-3} \lesssim y \lesssim 0.7$), and densities ($10^{-13}\,\mathrm{fm}^{-3} \lesssim n \lesssim 10\,\mathrm{fm}^{-3}$). This makes it easy to generate EOS tables covering the space in (n, T, y) required for simulations of CCSNe and NS mergers.

Using our new method, we generated EOS tables for nine Skyrme parametrizations: the L&S parametrization with $K_0 = 220\,\mathrm{MeV}$ (LS220) [3], NRAPR [59], SLy4 [73], SkT1 [71], SKRA [70], LNS [69], SQMC700 [74], Skxs20 [72] and KDE0v1 [68]. We thoroughly tested these EOSs, demonstrated thermodynamic consistency, and showed that our method can reproduce the results of the original L&S routines. We computed cold beta-equilibrated NS mass-radius relationships for all EOS and explored the ad-hoc high-density modifications that stiffen the EOS. We showed that these modifications can raise the maximum NS mass above the astrophysical lower limit of $2\,M_\odot$ while leaving EOS properties at saturation density largely unaffected.

As a first application of our new EOS tables to astrophysics simulations, we considered the spherically-symmetric collapse and postbounce CCSN evolution in 15-$M_\odot$ and 40-$M_\odot$ progenitor star models. We tracked the 40-$M_\odot$ models to black hole (BH) formation.

[5] Our method cannot presently handle Skyrme parametrizations that mix proton and neutron densities and kinetic energy densities in the nucleon effective masses (compare Equation 8 with Equation 5 of Dutra *et al.* [9]).

Comparing results from simulations with EOS tables relying on SNA at all (n, T, y) with those obtained with tables that match to NSE at low density, we find that SNA systematically, and independent of Skyrme parametrization, underpredicts the CCSN shock radius. Our analysis shows that the average heavy nucleus just outside the shock is predicted by SNA is almost always more bound than the nuclei present in the NSE mixture. Hence, the CCSN shock must do more work dissociating the average SNA nucleus, resulting in a smaller shock radius. The radius at which the shock stalls can have important ramifications for the CCSN explosion mechanism, which highlights the need for the more realistic NSE treatment at low densities that our new method provides.

In the case of BH formation, we find that the maximum proto-NS mass supported by a given EOS correlates with the maximum cold NS mass of the employed Skyrme parametrization, but is also highly sensitive to the treatment of the nucleon effective masses. The maximum proto-NS mass is typically substantially higher than the maximum cold NS mass due to thermal pressure support from compression-heated accreted outer core material. EOSs with lower effective nucleon masses lead to higher temperatures and thus more pressure support and a higher maximum proto-NS mass.

Our goal with this study was to build a new and robust method for generating finite-temperature nuclear EOS tables. These can facilitate CCSN and NS merger simulations that explore the sensitivity of these phenomena to EOS parameters and predict multi-messenger (neutrino, gravitational wave, nucleosynthetic) signatures whose observation could help constrain the EOS. We have realized this goal for the non-relativistic temperature-dependent liquid-drop model with Skyrme interaction. Much work lies ahead to generalize our method to include other mean-field parametrizations of nuclear interactions. A further important step will be to couple our new EOS tables to an efficient nuclear reaction network for accurately treating the regime in density, temperature, and composition space that is not in NSE.

Acknowledgments

We acknowledge helpful discussions with C. J. Horowitz, J. Lattimer, H. Nagakura, A. Ohnishi, and S. Richers. We thank Y. Suwa for pointing out that it is advantageous to preserve the precollapse pressure stratificiation when mapping stellar profiles into the core collapse code. A. S. S. was supported in part by the Conselho Nacional de Desenvolvimento Científico e Tecnológico (201432/2014-5). This research was also funded by the National Science Foundation under award No. AST-1333520, CAREER PHY-1151197, PHY-1404569, and by the Sherman Fairchild Foundation. C. D. O. thanks the Yukawa Institute for Theoretical Physics (YITP) for support and hospitality during the completion of this paper, which has been assigned report no. YITP-17-32.

Appendix A: Leptons and photons

We use the Timmes EOS to determine the properties of photons and leptons [93]. The only leptons considered here are electrons and positrons. The photon gas is assumed to be generated by a blackbody in local thermodynamic equilibrium. Its pressure, internal energy, and entropy are given by

$$P_{\rm rad} = \frac{4\sigma_{SB}T^4}{3c}\,, \quad E_{\rm rad} = 3P_{\rm rad}\,, \quad S_{\rm rad} = \frac{4E_{\rm rad}}{3T}\,, \tag{A1}$$

where σ_{SB} is the Stephan-Boltzmann constant, c the speed of light and n the baryon number density. The electron and positron contributions are determined assuming charge neutrality, *i.e.*,

$$yn = n_{\rm ele} - n_{\rm pos}\,. \tag{A2}$$

Recall that y is the proton fraction of the system. Here $n_{\rm ele}$ and $n_{\rm pos}$ are, respectively, the electron and positron number densities given by

$$n_{\rm ele} = K\beta^{3/2}\left[\mathcal{F}_{1/2}(\eta,\beta) + \mathcal{F}_{3/2}(\eta,\beta)\right]\,, \tag{A3a}$$

$$n_{\rm pos} = K\beta^{3/2}\left[\mathcal{F}_{1/2}(\kappa,\beta) + \mathcal{F}_{3/2}(\kappa,\beta)\right]\,, \tag{A3b}$$

where we define the constant $K = 8\pi\sqrt{2}m_e^3c^3/h^3$ with m_e being the electron mass. Furthermore, $\beta = T/(m_ec^2)$ is the relativity parameter, $\eta = \mu/T$ is the degeneracy parameter of electrons where μ is the electron chemical potential, and we define $\kappa = -\eta - 2/\beta$. The function $\mathcal{F}_k(\eta,\beta)$ is the Fermi-Dirac integral

$$\mathcal{F}_k(\eta,\beta) = \int_0^\infty \frac{u^k(1+0.5\beta u)^{1/2}}{1+\exp(u-\eta)}du\,. \tag{A4}$$

Note that the Fermi integral, Equation (10), is a special case of the Fermi-Dirac integral with $\beta = 0$. The degeneracy parameter η is found from the solution of Equation (A2) and can be used to obtain the thermodynamic variables of the electron and positron gas. Their pressures and energies per volume are given by

$$P_{\rm ele} = \frac{2K}{3}m_ec^2\beta^{5/2}\left[\mathcal{F}_{3/2}(\eta,\beta) + \frac{\beta}{2}\mathcal{F}_{5/2}(\eta,\beta)\right]\,, \tag{A5a}$$

$$P_{\rm pos} = \frac{2K}{3}m_ec^2\beta^{5/2}\left[\mathcal{F}_{3/2}(\kappa,\beta) + \frac{\beta}{2}\mathcal{F}_{5/2}(\kappa,\beta)\right]\,, \tag{A5b}$$

$$E_{\rm ele} = Km_ec^2\beta^{5/2}\left[\mathcal{F}_{3/2}(\eta,\beta) + \beta\mathcal{F}_{5/2}(\eta,\beta)\right]\,, \tag{A5c}$$

$$E_{\rm pos} = Km_ec^2\beta^{5/2}\left[\mathcal{F}_{3/2}(\kappa,\beta) + \beta\mathcal{F}_{5/2}(\kappa,\beta)\right] + 2n_{\rm pos}m_ec^2\,, \tag{A5d}$$

where the subscripts ele and pos refer, respectively, to electrons and positrons. Meanwhile, their entropy densities are

$$S_{\rm ele} = \frac{P_{\rm ele}+E_{\rm ele}}{T} - n_{\rm ele}\eta\,, \tag{A5e}$$

$$S_{\rm pos} = \frac{P_{\rm pos}+E_{\rm pos}}{T} - n_{\rm pos}\kappa\,. \tag{A5f}$$

For details on how these calculations are performed see [93].

Appendix B: Nuclear Statistical Equilibrium

In NSE, the chemical potential of nuclear species i is given by

$$\begin{aligned}\mu_i &= m_i + E_{c,i} + T\log\left[\frac{n_i}{g_i(T)}\left(\frac{2\pi}{m_i T}\right)^{3/2}\right], \\ &= Z_i\mu_p + (A_i - Z_i)\mu_n\,, \end{aligned} \tag{B1}$$

where m_i is the mass, A_i is the nucleon number, Z_i is the proton number, n_i is the number density, and $g_i(T)$ is the internal partition function of species i. We use the partition functions of Rauscher & Thielemann [97] and nuclear masses from the JINA REACLIB database. See Cyburt *et al.* [98] and references therein. The partition function tables and nuclear mass tables are available at http://stellarcollapse.org/SROEOS. The Coulomb correction in the Wigner-Seitz approximation is

$$E_{c,i} = \frac{3\alpha_C Z_i^2}{5r_i}\left(\frac{1}{2}u_i - \frac{3}{2}u_i^{1/3}\right), \tag{B2}$$

where the nuclear radius $r_i = (3A_i/4\pi n_s)^{1/3}$, $u_i = yn_b/n_sA_i/Z_i$, and α_C is the fine structure constant. Imposing mass and charge conservation, this system of equations can be solved for the composition. When calculating NSE, we assume that the neutrons and protons are arbitrarily degenerate, non-relativistic particles. We neglect Coulomb corrections for the protons.

The pressure, energy density, and entropy density of the nuclei ensemble in NSE is given by

$$P_n = \sum_i n_i\left\{T + \frac{\partial E_{c,i}}{\partial \ln n_b}\right\}, \tag{B3}$$

$$E_n = \sum_i n_i\left\{\frac{3}{2}T + E_{c,i} - \mathrm{B_i} + T\frac{d\ln g_i}{d\ln T}\right\}, \tag{B4}$$

$$S_n = \sum_i n_i\left\{\frac{5}{2} + \ln\left[\frac{g_i}{n_i}\left(\frac{m_iT_i}{2\pi}\right)^{3/2}\right] + \frac{d\ln g_i}{d\ln T}\right\} \tag{B5}$$

where $\mathrm{B_i}$ is the binding energy of species i relative to A_i neutrons. The contribution of the nucleons is given by the expressions in Section II A with the Skyrme parameters set to zero. The free energy density of the nuclei ensemble is set by

$$F_{\mathrm{NSE}} = E_n - TS_n. \tag{B6}$$

Appendix C: Critical temperature coefficients

In Section II B we present a method for determining the critical temperature T_c below which nuclear matter may phase separate into two phases of different densities, n_i and n_o, and proton fractions, y_i and y_o. In Table VIII, we present the coefficients calculated for the critical temperature approximation $T_c \equiv T_c(y_i)$, Equation (22). Since we do not obtain the surface properties for the LS220 parametrization, we set the coefficients $T_c(y_i)$ to match those of L&S. Note that for all other parametrizations we have $a_c \simeq 1.00$ and $b_c \simeq -1$. In fact, the EOS we calculate are not significantly altered by enforcing $a_c = 1$ and $b_c = -1$.

TABLE VIII: Coefficients for the fit of the proton-fraction dependence of the critical temperature $T_c(y)$ given by Equation (22). These coefficients depend on the Skyrme parametrization and we provide them here for completeness. T_c is in MeV while a_c, b_c, c_c, and d_c are dimensionless.

Parametrization	T_c	a_c	b_c	c_c	d_c
LS220 [3]	16.80	1.0000	−1.0000	0.0000	−0.0000
KDE0v1 [68]	14.85	1.0035	−1.1600	0.7797	−1.6822
LNS [69]	14.92	1.0017	−1.2052	0.2432	−0.6667
NRAPR [59]	14.39	1.0029	−1.0029	0.4679	−0.9929
SKRA [70]	14.35	1.0031	−1.1227	0.4336	−0.9523
SkT1 [71]	17.05	1.0022	−1.1921	0.4371	−0.7393
Skxs20 [72]	15.37	1.0017	−1.3778	0.4015	−0.6087
SLy4 [73]	14.52	1.0038	−1.0127	0.7771	−1.6520
SQMC700 [74]	14.72	1.0022	−1.1794	0.3284	−0.8968

[1] M. Oertel, M. Hempel, T. Klähn, and S. Typel, Rev. Mod. Phys. **89**, 015007 (2017).
[2] J. M. Lattimer and M. Prakash, Phys. Rep. **621**, 127 (2016).
[3] J. M. Lattimer and F. D. Swesty, Nucl. Phys. A **535**, 331 (1991).
[4] D. G. Ravenhall, C. J. Pethick, and J. M. Lattimer, Nucl. Phys. A **407**, 571 (1983).
[5] M. Hashimoto, H. Seki, and M. Yamada, Prog. Theor. Phys. **71**, 320 (1984).
[6] M. Prakash, I. Bombaci, M. Prakash, P. J. Ellis, J. M. Lattimer, and R. Knorren, Physics Reports **280**, 1 (1997).
[7] A. W. Steiner, M. Prakash, and J. M. Lattimer, Physics Letters B **509**, 10 (2001).
[8] J. A. Pons, S. Reddy, P. J. Ellis, M. Prakash, and J. M. Lattimer, Phys. Rev. C **62**, 035803 (2000).
[9] M. Dutra, O. Lourenço, J. S. Sá Martins, A. Delfino, J. R. Stone, and P. D. Stevenson, Phys. Rev. C **85**, 035201 (2012).
[10] M. Dutra, O. Lourenço, S. S. Avancini, B. V. Carlson, A. Delfino, D. P. Menezes, C. Providência, S. Typel, and J. R. Stone, Phys. Rev. C **90**, 055203 (2014).
[11] P. Demorest, T. Pennucci, S. Ransom, M. Roberts, and J. Hessels, Nature (London) **467**, 1081 (2010).
[12] J. Nättilä, A. W. Steiner, J. J. E. Kajava, V. F. Suleimanov, and

J. Poutanen, Astron. Astrophys. **591**, A25 (2016).
[13] J. M. Lattimer, Ann. Rev. Nucl. Part. Sci. **62**, 485 (2012).
[14] F. Özel and P. Freire, Ann. Rev. Astron. Astrophys. **54**, 401 (2016).
[15] J. M. Lattimer and M. Prakash, Astrophys. J. **550**, 426 (2001).
[16] Y. Lim, C. H. Hyun, and C.-H. Lee, to appear in Int. J. Mod. Phys. E; arXiv:1501.04397 (2015).
[17] I. Tews, J. M. Lattimer, A. Ohnishi, and E. E. Kolomeitsev, arXiv:1611.07133 (2016).
[18] K. Hebeler, J. M. Lattimer, C. J. Pethick, and A. Schwenk, Astrophys. J. **773**, 11 (2013).
[19] K. Hebeler, J. M. Lattimer, C. J. Pethick, and A. Schwenk, Phys. Rev. Lett. **105**, 161102 (2010).
[20] J. José and C. Iliadis, Rep. Prog. Phys. **74**, 096901 (2011).
[21] Z. Meisel, J. Phys. Conf. Ser. **742**, 012019 (2016).
[22] M. Wiescher, F. Käppeler, and K. Langanke, Ann. Rev. Astron. and Astrophys. **50**, 165 (2012).
[23] H. Schatz, J. Phys. G Nucl. Part. Phys. **43**, 064001 (2016).
[24] A. W. Steiner, M. Hempel, and T. Fischer, Astrophys. J. **774**, 17 (2013).
[25] R. Machleidt and D. R. Entem, Phys. Rep. **503**, 1 (2011).
[26] E. Rrapaj, A. Roggero, and J. W. Holt, Phys. Rev. C **93**, 065801 (2016).
[27] S. K. Bogner, R. J. Furnstahl, and A. Schwenk, Prog. Part. Nucl. Phys. **65**, 94 (2010).
[28] S. Gandolfi, A. Y. Illarionov, K. E. Schmidt, F. Pederiva, and S. Fantoni, Phys. Rev. C **79**, 054005 (2009).
[29] I. Sagert, G. I. Fann, F. J. Fattoyev, S. Postnikov, and C. J. Horowitz, Phys. Rev. C **93**, 055801 (2016).
[30] H. Shen, H. Toki, K. Oyamatsu, and K. Sumiyoshi, Nucl. Phys. A **637**, 435 (1998).
[31] J. R. Stone and P.-G. Reinhard, Prog. Part. Nucl. Phys. **58**, 587 (2007).
[32] G. Baym, H. A. Bethe, and C. J. Pethick, Nucl. Phys. A **175**, 225 (1971).
[33] D. Q. Lamb, J. M. Lattimer, C. J. Pethick, and D. G. Ravenhall, Phys. Rev. Lett. **41**, 1623 (1978).
[34] D. Q. Lamb, J. M. Lattimer, C. J. Pethick, and D. G. Ravenhall, Nucl. Phys. A **360**, 459 (1981).
[35] J. M. Lattimer, C. J. Pethick, D. G. Ravenhall, and D. Q. Lamb, Nucl. Phys. A **432**, 646 (1985).
[36] H. Shen, H. Toki, K. Oyamatsu, and K. Sumiyoshi, Prog. Theor. Phys. **100**, 1013 (1998).
[37] H. Shen, H. Toki, K. Oyamatsu, and K. Sumiyoshi, Astrophys. J. Suppl. Ser. **197**, 20 (2011).
[38] Y. Lim, Ph.D. thesis, Stony Brook University (2012), http://hdl.handle.net/11401/71321.
[39] S. I. Blinnikov, I. V. Panov, M. A. Rudzsky, and K. Sumiyoshi, Astron. Astrophys. **535**, A37 (2011).
[40] M. Hempel and J. Schaffner-Bielich, Nucl. Phys. A **837**, 210 (2010).
[41] M. Hempel, T. Fischer, J. Schaffner-Bielich, and M. Liebendörfer, Astrophys. J. **748**, 70 (2012).
[42] S. Furusawa, S. Yamada, K. Sumiyoshi, and H. Suzuki, Astrophys. J. **738**, 178 (2011).
[43] S. Furusawa, K. Sumiyoshi, S. Yamada, and H. Suzuki, Astrophys. J. **772**, 95 (2013).
[44] S. Furusawa, K. Sumiyoshi, S. Yamada, and H. Suzuki, Nucl. Phys. A **957**, 188 (2017).
[45] W. Hillebrandt, K. Nomoto, and R. G. Wolff, Astron. Astrophys. **133**, 175 (1984).
[46] W. Hillebrandt and R. G. Wolff, in *Nucleosynthesis: Challenges and New Developments*, edited by W. D. Arnett and J. W. Truran (University of Chicago Press, 1985), p. 131.
[47] G. Shen, C. J. Horowitz, and S. Teige, Phys. Rev. C **82**, 015806 (2010).
[48] G. Shen, C. J. Horowitz, and S. Teige, Phys. Rev. C **82**, 045802 (2010).
[49] G. Shen, C. J. Horowitz, and S. Teige, Phys. Rev. C **83**, 035802 (2011).
[50] E. O'Connor and C. D. Ott, Class. Quantum Grav. **27**, 114103 (2010).
[51] E. O'Connor and C. D. Ott, Astrophys. J. **730**, 70 (2011).
[52] E. O'Connor, Astrophys. J. Suppl. Ser. **219**, 24 (2015).
[53] A. Burrows and J. M. Lattimer, Astrophys. J. **285**, 294 (1984).
[54] C. J. Horowitz and A. Schwenk, Nucl. Phys. A **776**, 55 (2006).
[55] B. K. Agrawal, S. K. Dhiman, and R. Kumar, Phys. Rev. C **73**, 034319 (2006).
[56] N. Chamel, S. Goriely, and J. M. Pearson, Phys. Rev. C **80**, 065804 (2009).
[57] T. Fukushima, Appl. Math. Comput. **259**, 698 (2015).
[58] T. Fukushima, Appl. Math. Comput. **259**, 708 (2015).
[59] A. W. Steiner, M. Prakash, J. M. Lattimer, and P. J. Ellis, Phys. Rep. **411**, 325 (2005).
[60] J. M. Lattimer and D. G. Ravenhall, Astrophys. J. **223**, 314 (1978).
[61] K. Nakazato, K. Iida, and K. Oyamatsu, Phys. Rev. C **83**, 065811 (2011).
[62] H. Pais and J. R. Stone, Phys. Rev. Lett. **109**, 151101 (2012).
[63] B. Schuetrumpf, M. A. Klatt, K. Iida, G. E. Schröder-Turk, J. A. Maruhn, K. Mecke, and P.-G. Reinhard, Phys. Rev. C **91**, 025801 (2015).
[64] D. G. Ravenhall, C. J. Pethick, and J. R. Wilson, Phys. Rev. Lett. **50**, 2066 (1983).
[65] R. D. Woods and D. S. Saxon, Phys. Rev. **95**, 577 (1954).
[66] B. Hasselman, *Package "nleqslv"* (2016), URL https://cran.r-project.org/web/packages/nleqslv/index.html.
[67] J. R. Stone, J. C. Miller, R. Koncewicz, P. D. Stevenson, and M. R. Strayer, Phys. Rev. C **68**, 034324 (2003).
[68] B. K. Agrawal, S. Shlomo, and V. K. Au, Phys. Rev. C **72**, 014310 (2005).
[69] L. G. Cao, U. Lombardo, C. W. Shen, and N. V. Giai, Phys. Rev. C **73**, 014313 (2006).
[70] M. Rashdan, Mod. Phys. Lett. A **15**, 1287 (2000).
[71] F. Tondeur, M. Brack, M. Farine, and J. Pearson, Nucl. Phys. A **420**, 297 (1984).
[72] B. A. Brown, G. Shen, G. C. Hillhouse, J. Meng, and A. Trzcińska, Phys. Rev. C **76**, 034305 (2007).
[73] E. Chabanat, P. Bonche, P. Haensel, J. Meyer, and R. Schaeffer, Nucl. Phys. A **635**, 231 (1998).
[74] P. A. M. Guichon, H. H. Matevosyan, N. Sandulescu, and A. W. Thomas, Nucl. Phys. A **772**, 1 (2006).
[75] A. Bauswein, S. Goriely, and H.-T. Janka, Astrophys. J. **773**, 78 (2013).
[76] K. Taniguchi and M. Shibata, Astrophys. J. Suppl. Ser. **188**, 187 (2010).
[77] P. J. Mohr, D. B. Newell, and B. N. Taylor, Rev. Mod. Phys. **88**, 035009 (2016).
[78] R. C. Tolman, Phys. Rev. **55**, 364 (1939).
[79] J. Antoniadis et al., Science **340**, 6131 (2013).
[80] R. B. Wiringa, V. G. J. Stoks, and R. Schiavilla, Phys. Rev. C **51**, 38 (1995).
[81] R. Machleidt, Phys. Rev. C **63**, 024001 (2001).
[82] V. G. J. Stoks, R. A. M. Klomp, C. P. F. Terheggen, and J. J. de Swart, Phys. Rev. C **49**, 2950 (1994).
[83] E. Fonseca, T. T. Pennucci, J. A. Ellis, I. H. Stairs, D. J. Nice, S. M. Ransom, P. B. Demorest, Z. Arzoumanian, K. Crowter,

T. Dolch, et al., Astrophys. J. **832**, 167 (2016).
[84] J. M. Lattimer and A. W. Steiner, Astrophys. J. **784**, 123 (2014).
[85] S. Guillot, M. Servillat, N. A. Webb, and R. E. Rutledge, Astrophys. J. **772**, 7 (2013).
[86] J. R. Stone, P. A. M. Guichon, H. H. Matevosyan, and A. W. Thomas, Nucl. Phys. A **792**, 341 (2007).
[87] W. R. Hix, O. E. B. Messer, A. Mezzacappa, M. Liebendörfer, J. Sampaio, K. Langanke, D. J. Dean, and G. Martínez-Pinedo, Phys. Rev. Lett. **91**, 201102 (2003).
[88] S. R. Souza, A. W. Steiner, W. G. Lynch, R. Donangelo, and M. A. Famiano, Astrophys. J. **707**, 1495 (2009).
[89] M. Liebendörfer, Astrophys. J. **633**, 1042 (2005).
[90] F. D. Swesty, J. Comp. Phys. **127**, 118 (1996).
[91] S. E. Woosley and T. A. Weaver, Astrophys. J. Suppl. Ser. **101**, 181 (1995).
[92] S. E. Woosley and A. Heger, Phys. Rep. **442**, 269 (2007).
[93] F. X. Timmes and D. Arnett, Astrophys. J. Suppl. Ser. **125**, 277 (1999).
[94] S. E. Woosley, A. Heger, and T. A. Weaver, Rev. Mod. Phys. **74**, 1015 (2002).
[95] R. Buras, M. Rampp, H.-T. Janka, and K. Kifonidis, Astron. Astrophys. **447**, 1049 (2006).
[96] C. Thompson, Astrophys. J. **534**, 915 (2000).
[97] T. Rauscher and F.-K. Thielemann, At. Data Nucl. Data Tables **75**, 1 (2000).
[98] R. H. Cyburt, A. M. Amthor, R. Ferguson, Z. Meisel, K. Smith, S. Warren, A. Heger, R. D. Hoffman, T. Rauscher, A. Sakharuk, et al., Astrophys. J. Suppl. Ser. **189**, 240 (2010).